Separation and Transition on a Cone-Cylinder-Flare: Computational Investigations

Clément Caillaud *
CEA-CESTA, 15 Avenue des Sablières, Le Barp, France

Anton Scholten†
North Carolina State University, Raleigh, NC, 27695

Joseph Kuehl‡
University of Delaware 130 Academy Street, DE 19726

Pedro Paredes§
National Institute of Aerospace, Hampton, VA 23666

Mathieu Lugrin¶
DAAA, ONERA, Université Paris Saclay, F-92190 Meudon - France

Sébastien Esquieu ‖
CEA-CESTA, 15 Avenue des Sablières, Le Barp, France

Fei Li** and Meelan M. Choudhari††
NASA Langley Research Center, Hampton, VA, 23681

Elizabeth K. Benitez‡‡ and Matthew P. Borg§§
U.S. Air Force Research Laboratory, Wright-Patterson AFB, OH 45433

Zachary A. McDaniel¶¶ and Joseph S. Jewell***
Purdue University, West Lafayette, IN, 47907

Base flow computation and stability analysis were conducted for hypersonic flow over a cone-cylinder-flare (CCF) geometry for conditions that correspond to the experimental runs carried out in three wind tunnels. Owing to the presence of an attached boundary layer, a separation bubble induced by a shock-boundary layer interaction, and a reattachment region, the chosen flow configuration is physically rich. The complexity of this flowfield encompasses a combination of convective instabilities developing on the cone, global instabilities in the separation bubble, and shear-layer modes and streaks in the reattachment region. Thus, the selected CCF configuration provides the opportunity for a comprehensive comparison of the currently available methodologies for analyzing boundary layer instabilities. Various tools are used for the analysis, including global stability codes as well as convective instability analyses based on a local theory, a weakly non-parallel analysis, and tools that are applicable to strongly

*Research Engineer
†Graduate Student, Department of Mechanical and Aerospace Engineering, AIAA Student Member
‡Associate Professor, Mechanical Engineering, AIAA Member
§Associate Research Fellow, Computational AeroSciences Branch, NASA LaRC, AIAA Senior Member
¶Research Engineer
‖Research Engineer
**‡Aerospace Technologist, Computational AeroSciences Branch
††Aerospace Technologist, Computational AeroSciences Branch, AIAA Fellow
‡‡Research Aerospace Engineer, Hypersonic Sciences Branch, elizabeth.benitez.2@us.af.mil, AIAA Member
§§Senior Aerospace Engineer, Hypersonic Sciences Branch, AIAA Associate Fellow
¶¶Graduate Student, School of Aeronautics and Astronautics, AIAA Student Member
***John Bogdanoff Associate Professor, School of Aeronautics and Astronautics, AIAA Associate Fellow
Distribution Statement A: Approved for Public Release; Distribution is Unlimited. PA# AFRL-2023-5756; Cleared 11/13/2023.

non-parallel flows. The paper presents a comparison of the convective instability characteristics based on different methodologies, such as linear stability theory (LST), the harmonic form of linearized Navier-Stokes equations (HLNSE), and resolvent analysis. The CCF configuration provided an effective framework for conducting a detailed cross-validation of this type, which had not yet been addressed in existing literature. This document is accompanied by a companion paper that is focused on the experimental aspects of the CCF configuration. Both papers are being presented in a dedicated session that highlights the research activities of the NATO STO Research Task Group AVT-346.

Nomenclature

C_p	=	specific heat (J(kg K)$^{-1}$)
c	=	wave speed (m s^{-1})
HLNSE	=	harmonic linearized Navier-Stokes equations
M	=	Mach number
P	=	pressure (Pa)
PSD	=	power spectral density
q''	=	heat transfer (W/m^2)
Re_∞	=	unit freestream Reynolds number (m^{-1})
Re_x	=	axial length Reynolds number
St	=	Stanton number
T_0	=	stagnation temperature (K)
T_w	=	wall temperature (K)
u_x	=	streamwise velocity (m s^{-1})
R_n	=	nose radius (mm)
Δ	=	change in quantity
μ	=	dynamic viscosity (kg(m s)$^{-1}$)
ρ	=	density (kg m^{-3})
f	=	frequency (s^{-1})
ω	=	angular frequency, $(2\pi f)$
m	=	azimuthal wavenumber
$(\bullet)_\infty$	=	freestream values
$(\bullet)_e$	=	boundary layer edge values
$\boldsymbol{q}$	=	state vector

I. Introduction

Understanding boundary layer transition remains a primary challenge in the advancement of hypersonic flight due to its significant impact on vehicle design. This challenge is further heightened when dealing with flows involving shock-boundary layer interactions (SBLI). Such flows present transitional mechanisms that are not fully understood, as various types of disturbance amplification mechanisms can influence the flow behavior. To address this challenge, the cone-cylinder-flare (CCF) geometry was designed in early 2020. The goal of this design is to provide a flow topology that can capture several types of instability processes found in atmospheric reentry vehicles [1], including both absolute and convective instabilities. Since then, multiple studies, either experimental [2, 3], or numerical [4] have started to unveil the dominant transition mechanisms present in the CCF flow. Multiple convective instabilities may play a role in the transition process in different regions of the CCF flow. Starting on the cone, oblique first-mode and second-mode may undergo significant amplification, especially for a sharp nosetip, with the second-mode disturbances representing the dominant instability. As the flow proceeds through an expansion fan at the cone-cylinder junction, the energy of these instabilities is reduced [5]. Further downstream, the flow encounters the shock wave arising from the compression of the flow near the start of the flare. Depending on the state of the boundary layer approaching the cylinder-flare

junction, the boundary layer flow may undergo separation, creating a recirculation bubble that may support numerous unstable global modes past a critical value of the Reynolds number [6–8]. The onset of separation also leads to the formation of a mixing layer that can support shear-layer instabilities related to the first-mode disturbances in an attached boundary layer [9, 10]. Downstream of the separation, the flow undergoes reattachment that is associated with flow compression and is known to strongly amplify linear instabilities and is often found to trigger a rapid transition to turbulence. One pivotal feature of such separated flows is the strong coupling between the existence and the size of the recirculation region and the process of laminar-turbulent transition [10, 11]. This coupling is known to induce a reduction in the size of the recirculation bubble that is proportional to the intensity of the incoming flow disturbances. Finally, In relation to the separated flow, a last feature of interest is the presence of heat-flux streaks following the reattachment on the flare. Multiple origins inducing the growth of these streaks have been found. These factors can be attributed to either the saturation of global modes [6], or convective baroclinic effects [12], or nonlinear mechanisms [10]. It is essential to remember that apart from the global modes, all other instabilities mentioned above are convective in nature. The convective modes are first seeded by the freestream noise through the receptivity process, after which they undergo linear amplification until they attain an amplitude sufficient to initiate nonlinear saturation. This, in turn, can ultimately trigger the onset of transition.

Given the intricate instability dynamics over the CCF geometry with a 12° flare angle (CCF12 [13]), the present study describes a joint multinational effort within the NATO STO AVT-346 Research Task Group that analyzed the linear instability characteristics of the CCF flowfield at $M_\infty = 6.0$ and compared the computational predictions with the recent experimental studies published in a companion paper [14]. The present investigation targets several distinct goals. The first is to cross-validate both the Navier-Stokes solvers used to compute the laminar base flows and the associated codes that would be used to analyze the linear stability of those flows. Such a code-to-code comparison is still lacking in the literature on laminar hypersonic flows with shock boundary-layer interactions and remains a fundamental step in reliable predictions of the physics of the linear instability mechanisms at play in those flows. An exercise of this type is especially important for the CCF configuration, because traditional tools such as linear stability theory (LST) or the parabolized stability equations (PSE) are based on the assumption of a parallel or weakly non-parallel basic state, and may therefore be inaccurate due to the strong non-parallel effect in the separated region. Additionally, transient growth mechanisms that are impossible to capture using local modal analysis, such as the lift-up effect, may play a role in the amplification of streaks and are yet to be taken into consideration within a comparative assessment of this type. Due to the abovementioned limitations of LST and PSE, it becomes necessary to employ new, higher-fidelity tools that fully account for the dynamics of the linear Navier-Stokes operator without imposing additional constraints on the disturbance field besides its linearity. Multiple theoretical frameworks have emerged to address this need, including the Harmonic Linearized Navier-Stoked Equations (HLNSE), global Input-Output analysis (I/O), or the resolvent analysis. Such tools, although computationally expensive, are becoming increasingly commonplace in the literature on hypersonic transition. However, very few comparisons and cross-validations between the different techniques have been presented to date.

The second goal of the present research is directly tied to the physics of the instability mechanisms on the CCF configuration, namely, to investigate and map the dominant instabilities at selected flow conditions from the wind tunnel experiments conducted within the same joint effort [14]. In addition to investigating the global modes originating from the recirculation bubble, the current study also examines the convective instabilities. This allows us to first confirm the ability of the linear approach to capture the physics at play in the experiments and then to further investigate the mechanisms seen in the transition process over such geometry. With these goals in mind, the CCF configurations considered here include both nominally sharp (0.1 mm) and moderately blunt (5 mm) nose radius in order to allow for the effects of nosetip bluntness to be assessed.

This outline of this article is as follows. First, the CCF geometry and a summary of the typical baseflow features are presented. In the third section, all the numerical and stability methods are described. Using these methodologies, the fourth section describes the cross-validation of NASA and ONERA/CEA codes for the baseflow computations, with an emphasis on the grid requirements. The fifth section is dedicated to the linear analysis of the instabilities at play in the sharp and blunt cases. The last section compares the computed linear dynamics with the experimental data collected in conventional and quiet wind tunnels, with a consideration of the possible receptivity effects. The final section presents a summary of the results and outlines the conclusions.

II. CCF Geometry and Sample Baseflows

This section provides an introduction to the CCF configuration and sets the stage for the cross-validation study described in Sec. IV. The two CCF configurations of interest are based on the experiments performed in both French and

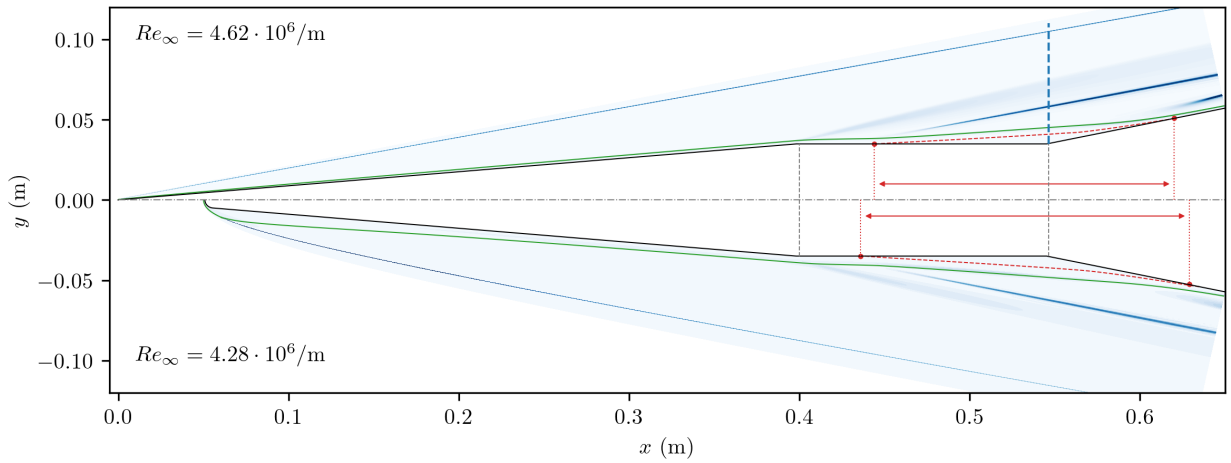

Fig. 1 Baseflow for the $R_n = 0.1$mm (top) and $R_n = 5$mm (bottom) CCF12 geometries. Greyscale: normalized numerical shadowgraphy with —: entropy layer; - - : recirculation bubble with separation and reattachment points (•); —: line along which the profiles of Fig. 4 are extracted.

American wind tunnels [14] during the activities of the Research Task Group NATO-AVT-346. These configurations are denoted as CCF10 and CCF12, representing flare angles of 10° and 12°, respectively. The upstream segment of the CCF geometry consists of a 5° half-angle cone that is followed by a 147 mm long cylinder with a diameter of 70 mm. Downstream of the cylinder is a flare section with an angle of 10 or 12 degrees, extending until the total model diameter reaches 114 mm. Sharp and blunt nosetips of radius $R_n = 0.1$ mm and $R_n = 5$ mm are identified as R01 and R05, respectively. These geometrical parameters are summarized in Tab. 1.

Sample baseflows $\boldsymbol{q}_0$ for CCF12 cases R01 and R05 at $Re_\infty = 4.6 \times 10^6$ m^{-1} are shown in the top and bottom halves, respectively, of Fig. 1. A comparison between the flow features for the R01 and R05 cases reveals the two main differences resulting from the change in the nosetip radius. First, the larger nose radius in case R05 leads to a greater shock stand-off distance, which in turn leads to a thicker entropy layer that propagates farther downstream with a swallowing point close to the cone cylinder junction. For the R01 case, the entropy layer remains thin and closely follows the boundary layer height. Larger entropy layers are known to reduce or even suppress the growth of both first- and second-mode instabilities [15, 16]; thus, different behavior of the linear instabilities is expected for the R01 and R05 cases. These differences will be further investigated in the subsequent sections. The second noticeable difference between the two cases is the length of the separation bubble near the cylinder-flare junction. The R05 case displays a larger separated region, potentially as a result of the thicker boundary layer in that case. This behavior has already been observed on compression ramps [17] and the moderate bluntness effect is known to increase the size of the separated region. Given the strong likelihood of a global instability in the region of flow separation, we first investigate the global stability characteristics of the CCF flowfield. The associated numerical tools are introduced in the following section.

Parameter	Value
L_{cone}	398.2 mm
L_{cyl}	147.3 mm
L_{flare}	104.9 mm
R_n	0.1 mm or 5 mm
θ_{cone}	5°
θ_{flare}	12°

Table 1 Main geometrical parameters of the CCF12 geometry

III. Numerical Frameworks

A description of the various numerical methodologies applied to the CCF configurations of interest is provided in this section. Section III.A presents the governing equations in cylindrical coordinates, along with the linearized form of those equations. In Section III.B, the framework for the Resolvent analysis in a global context is detailed, and Section III.C outlines the harmonic form of the linearized Navier-Stokes equations (HLNSE) and the linear stability theory (LST), which are used to analyze the evolution of convective instabilities over the $R_n = 0.1$ mm nosetip. The approach used is a combination of the linear parabolized stability equations (PSE) and the HLNSE frameworks. For the $R_n = 5$ mm nosetip, nonmodal analysis is performed using the HLNSE as modal (in the local sense) amplification is not found to be present.

A. Governing equations

Considering the geometry of the CCF configuration in an axisymmetric frame, the cylindrical coordinates (x, r, θ) are utilized throughout this work. The computational domain is discretized in a structured fashion with a total of N_c cells. The flow dynamics are governed by the following discrete, nonlinear dynamical system,

$$\frac{\partial \boldsymbol{q}}{\partial t} = \boldsymbol{N}(\boldsymbol{q}) + \boldsymbol{f}, \tag{1}$$

where $\boldsymbol{q}$ is the conservative state vector of N_v variables, $\boldsymbol{N}$ is the discrete (i.e., for a given numerical method on a given mesh) compressible Navier-Stokes operator, and $\boldsymbol{f}$ is a harmonic exogenous forcing of small amplitude. Supposing the existence of a fixed-point $\boldsymbol{q}_0$ (i.e., steady state) such that $\boldsymbol{N}(\boldsymbol{q}_0) = 0$, the non-linear system can be linearized around this steady state in order to retrieve the linear dynamics of small disturbances $\boldsymbol{q}'$, with $\boldsymbol{q} = \boldsymbol{q}_0 + \epsilon \boldsymbol{q}'$, $\epsilon \ll 1$. The linear disturbance equations can be written as,

$$\frac{\partial \boldsymbol{q}'}{\partial t} = \mathbf{L}\boldsymbol{q}' + \boldsymbol{f}, \quad \text{with } \mathbf{L} = \left.\frac{\partial \boldsymbol{N}(\boldsymbol{q})}{\partial \boldsymbol{q}}\right|_{\boldsymbol{q}_0}, \tag{2}$$

where $\mathbf{L}$ denotes the Jacobian of the nonlinear operator around $\boldsymbol{q}_0$. For further details about the global linear dynamics, the reader is referred to the comprehensive review of [18].

Given that this study is limited to a zero-degrees angle of attack, the unperturbed laminar basic state may be considered to be axisymmetric. Hence, linear disturbances can be expressed in terms of their frequency ω and azimuthal wavenumber m. Depending on the simplifying hypotheses made concerning the streamwise evolution of the flow, different expressions of the disturbance vectors can be considered:

Hypothesis	Expression
Locally parallel	$\boldsymbol{q}'(r,\theta,t) = \hat{\boldsymbol{q}}(x) e^{i(\alpha x + m\theta + \omega t)} + c.c$
Weakly non-parallel	$\boldsymbol{q}'(x,r,\theta,t) = \hat{\boldsymbol{q}}(x,r) e^{i\left(\int_{x_0}^{x} \alpha(x')dx' + m\theta + \omega t\right)} + c.c$
Global	$\boldsymbol{q}'(x,r,\theta,t) = \hat{\boldsymbol{q}}(x,r) e^{i(m\theta + \omega t)} + c.c$

Table 2 Summary of the disturbance forms considered for comparison.

B. Global Stability and Resolvent framework

The analysis is supported by the stability toolbox BROADCAST [19] from ONERA. It uses high-order finite-volume schemes [20] and algorithmic differentiation [21] to compute the fixed points of the compressible Navier-Stokes equations. After that, it extracts the associated direct and adjoint global linear operators, including their derivatives up to the desired order.

Using this toolbox, and considering a three-dimensional evolution of the flow, the linear dynamics of Eq. 2 will be studied in two ways. The first approach considers the autonomous system, i.e., $\boldsymbol{f} = 0$. In Fourier space, the global stability of the baseflow at a given frequency, ω, and wavenumber, m, can be studied by solving the eigenvalue problem (EVP),

$$\mathbf{L}(m)\hat{\boldsymbol{q}} = i\lambda\hat{\boldsymbol{q}}, \quad \lambda = \sigma + i\omega, \tag{3}$$

where λ denotes the complex eigenvalue. Hence, the growth rate of an eigenfunction corresponds to $\Re(\lambda) = \sigma$, and the associated frequency is given by $\Im(\lambda) = \omega$.

Additionally, the evolution of disturbances can be studied for the forced system, i.e., $\boldsymbol{f} \neq 0$. Due to the non-normality of the Jacobian operator $\mathbf{L}$, exogenous forcing may trigger nonmodal amplification of convective instabilities even if the system is globally stable [22]. These amplification mechanisms can be studied using the resolvent operator defined as $\boldsymbol{\mathcal{R}} = (i\omega\mathbf{I} - \mathbf{L})^{-1}$. For noise-amplifier flows, this operator yields an input-output relation between the forcing at a given frequency and azimuthal wavenumber and the resulting response of the baseflow $\boldsymbol{q}_0$, such that,

$$\hat{\boldsymbol{q}} = \boldsymbol{\mathcal{R}}(\omega, m)\hat{\boldsymbol{f}}, \quad \omega \in \mathbb{R}. \tag{4}$$

To find the most amplified convective instabilities for a given pair of (ω, m) values, one computes an optimal decomposition of rank $N_r = N_c \times N_v$ for the resolvent matrix. This provides an orthogonal basis of optimal forcings $\boldsymbol{\phi}_i$ and responses $\boldsymbol{\psi}_i$ that are ranked by energy. Starting from Eq. 4, we introduce an arbitrary forcing vector $\hat{\boldsymbol{\phi}}_i$ and its associated response vector $\hat{\boldsymbol{\psi}}_i$, and employ the discrete norms denoted as $||\hat{\boldsymbol{\psi}}||_E = \hat{\boldsymbol{\psi}}^* \mathbf{W}_E \hat{\boldsymbol{\psi}}$ and $||\hat{\boldsymbol{\phi}}||_F = \hat{\boldsymbol{\phi}}^* \mathbf{P}^* \mathbf{W}_f \mathbf{P} \hat{\boldsymbol{\phi}}$, where $\mathbf{W}_E$ and $\mathbf{W}_F$ correspond to the Chu energy weight matrix [23] and $\mathbf{P}$ is the restriction matrix used to impose the forcing on specific regions or variables. This formulation is used to evaluate the Rayleigh quotient,

$$\mu_0^2 = \sup_{\hat{\boldsymbol{\phi}}} \frac{||\hat{\boldsymbol{\psi}}||_E}{||\hat{\boldsymbol{\phi}}||_F} = \sup_{\hat{\boldsymbol{\phi}}} \frac{||\boldsymbol{\mathcal{R}}\hat{\boldsymbol{\phi}}||_E}{||\hat{\boldsymbol{\phi}}||_F}. \tag{5}$$

The optimal forcing that satisfies equation 5 may then be found by solving the eigenvalue problem:

$$\mathbf{P}^* \boldsymbol{\mathcal{R}}^* \mathbf{W}_E \boldsymbol{\mathcal{R}} \mathbf{P} \boldsymbol{\phi}_i = \mu_i^2 \mathbf{W}_f \boldsymbol{\phi}_i, \tag{6}$$

where $(\bullet)^*$ is the Hermitian transpose and the eigenvalues $\mu_0^2 > ... > \mu_i^2 > \mu_{i+1}^2 > ...$ of Eq. 6 are the optimal gains ranked by energy and their associated eigenfunctions $\boldsymbol{\phi}_i$ are the optimal forcings. Solving Eq. 6 for various values of (ω, m) allows one to map the system amplification peaks.

C. PSE/HLNSE framework

The HLNSE and PSE frameworks describe the streamwise evolution of time harmonic, convective instability waves in a given basic flow. The HLNSE are valid for all possible basic states, whereas the PSE are limited to base flows that are at most weakly non-parallel. The HLNSE are obtained from the linear form of the perturbation equations by invoking the "global" ansatz from Tab. 2 and are given by

$$(\mathbf{L}(m) - i\omega)\hat{\boldsymbol{q}} = \hat{\boldsymbol{f}}, \tag{7}$$

In this case, the vector of dependent variables $\hat{\boldsymbol{q}}$ must resolve both the shorter length scales associated with the rapid phase and amplitude variations corresponding to the convective instability waves and the (usually) slower modulation associated with the non-parallelism of the mean flow. On the other hand, the linear form of the PSE [24] is obtained by using the perturbation ansatz from Table 2 that corresponds to weakly non-parallel flows, then imposing a constraint that absorbs the rapid phase variations along the streamwise direction within the exponential term involving α, and finally, by dropping the viscous terms associated with streamwise diffusion. Under suitable conditions, the resulting set of equations can be solved by marching along the streamwise direction. The decomposition between an exponential term representing the short-scale variations in the perturbation field and the shape function $\hat{\boldsymbol{q}}$ is made unique by imposing an integral constraint. Further details about the HLNSE and PSE implementations can be found in Refs. [25, 26]. High-order finite-difference schemes of sixth order are used to discretize the stability equations on a non-uniform grid along the wall-normal direction. The HLNSE are discretized with a sixth-order, central scheme along the streamwise direction, whereas the PSE are discretized with a second-order backward difference. The boundary conditions used to solve both sets of equations are similar to those used in the resolvent framework and are detailed in a subsequent section.

D. Nonmodal analysis

Given the rapid streamwise variations induced by the flare, it is appropriate to employ the HLNSE for the nonmodal analysis. The optimal initial disturbance, $\tilde{\mathbf{q}}_0$, is defined as the initial (i.e., inflow) condition at ξ_0 that maximizes the objective function, J, which is defined as a measure of disturbance growth over a specified interval $[\xi_0, \xi_1]$. The definition used in the present study corresponds to the outflow energy gain Ref. [27, 28] that is defined as

$$G = \frac{E(\xi_1)}{E(\xi_0)}. \tag{8}$$

The variational formulation of the problem to determine the maximum of the objective functional J leads to an optimality system [29], which is solved in an iterative manner, starting from a random solution at ξ_0 that must satisfy the boundary conditions. The HLNSE, $\mathbf{L}\tilde{\mathbf{q}} = \mathbf{0}$, are used to integrate $\tilde{\mathbf{q}}$ up to ξ_1, where the final optimality condition is used to obtain the initial condition for the adjoint equations integration, $\mathbf{L}^\dagger\tilde{\mathbf{q}}^\dagger = 0$.

IV. Cross-Validation of Baseflow Computations

This section covers the cross-comparisons of the baseflows using two different solvers. It is organized as follows: First, we outline the numerical schemes employed by the solver as well as the boundary conditions used in the base flow computations. Next, in section IV.B, we present a grid convergence study for the same CCF10 case as Ref. [26]. Then, the freestream conditions for the CCF12 configurations explored in this paper are presented in section IV.C, together with a comparison of the laminar basic states computed by the two solvers. Following the cross-validation of the laminar base flow, the global stability results are compared, and the most unstable modes are presented in section V.A. The PSE and HLNSE combined results are compared with the predictions of the resolvent analysis and the amplification of convective instabilities supported by the laminar basic states over the CCF configurations of interest are given in section V.B. A local instability analysis for the CCF configuration is also performed in section V.C. Finally, nonmodal analysis results for the blunt nosetip are provided in section V.B

A. Numerical schemes and boundary conditions

The base flows are obtained from two different numerical solvers named VULCAN-CFD* and BROADCAST†, which correspond to the computations from NASA and CEA-ONERA, respectively. BROADCAST uses finite-volume spatial schemes with a convective fluxes reconstruction of order 7 [20] and a centered viscous fluxes reconstruction of order 4, coupled with a pseudo-transient continuation technique [30] to perform Newton iterations of the non-linear Navier-Stokes operator, the initial transient can also be time marched beforehand using an implicit local time-stepping solver. On the other hand, VULCAN-CFD uses 4th-order finite-volume schemes coupled with an implicit time stepper. For each code, more details about the numerical methods can be found in Ref. [31–33] and Ref. [19]

Along with the numerical methods, the domain is taken as a 2D plane containing the entire CCF12 geometry and the region upstream of the detached shock. The wall boundary is taken isothermal with $T_w = 300$ K. The grid fully resolves the nosetip for both value of R_n. Considering supersonic incoming flow, the farfield upstream of the shock is taken as a Dirichlet boundary condition with by enforcing a state vector $\boldsymbol{q}_\infty$ computed from the freestream conditions given in Tab. 3. The border at the nosetip following the line $y = 0$ is defined as an axisymmetric boundary condition, enforcing the correct symmetry and antisymmetry rules on the normals and conservative variables. Finally, considering the flow to be mostly supersonic in the shock layer, the outflow boundary condition is taken as an extrapolation of order 0 by extending the last-cell conservative variables values to the ghost-cells. The boundary conditions are consistent across the two numerical frameworks. Grid definitions are however different and are further discussed in the following sections.

B. Assessing grid requirements for global stability

To assess the impact of grid refinement on stability results, multiple computations on successively refined grids are computed using BROADCAST. The obtained results are compared against some previous reference computations for a CCF10 case at $Re_\infty = 11.5 \times 10^6$ m^{-1} [26]. The initial BROADCAST baseflow is computed using a shock-aligned grid of size $N_x \times N_y = 1340 \times 400$ over the full geometry. Using the boundary layer height from a preliminary computation, the mesh is refined within the boundary and shear layers. The streamwise evolution of the grid is defined by two factors: the number of grid points along the nosetip $N_{x,tip}$ and along the cylinder $N_{x,cyl}$. Then, a slow linear growth of the cell size on the cone is imposed until it reaches the cylinder with a cell size matching condition implicitly imposed by the $N_{x,cyl}$ parameter. Downstream of the cylinder, the streamwise cell size is kept constant. Starting from a preliminary solution obtained via interpolation, around twelve Newton iterations are usually necessary to reach residuals magnitude close to machine-precision with values typically equal to: $(||\mathbf{N}(\boldsymbol{q}_0)||_{L_2} \leq 10^{-12})$.

With the baseflow obtained in this manner, the EVP given in Eq. 3 is restricted to the aft portion of the geometry containing the separated flow. This region starts slightly upstream of the cone-cylinder junction ($x > 0.38$), extends until the end of the flare, and contains the full domain height. Figure 2a shows the predicted eigenvalue spectrum in the growth rate-azimuthal wavenumber plane, along with a comparison against the reference predictions reprinted from [4]

*visit `http://vulcan-cfd.larc.nasa.gov` for further information about the VULCAN-CFD solver

†For more details about this open-source ONERA solver, visit `https://github.com/onera/Broadcast`.

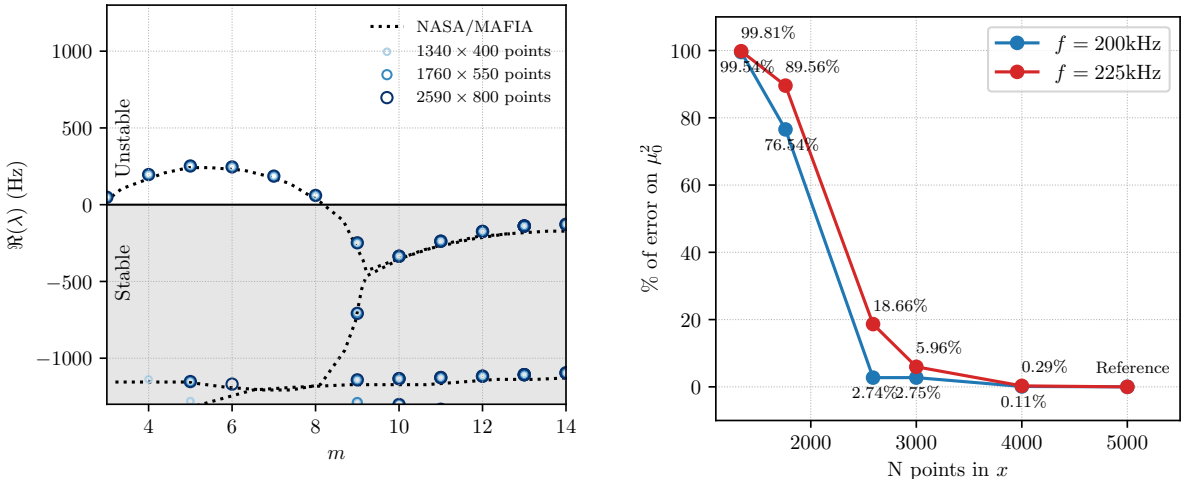

(a) Global spectrum convergence. **(b) Resolvent mode convergence**

Fig. 2 Growth rates of the global modes of the separation bubble on the CCF10-R01 configuration as functions of m. The plotted spectra include a grid convergence study (indicated by colored symbols) as well as a comparison with the computed spectra from Ref. [34]

in dotted lines, which were calcualted with the NASA Langley Research Center MAtrix Forming Instability Analysis (MAFIA) solver. The discrete azimuthal modes computed from the BROADCAST baseflows are shown in blue circles for grid sizes ranging from $N_x \times N_y = 1340 \times 400$ up to $N_x \times N_y = 2590 \times 800$. Overall, the computation shows a near-perfect agreement between the two numerical frameworks. Four main branches can be observed, with an unstable one corresponding to steady modes of azimuthal wavenumber $m \in [0, 8]$. The mesh convergence also indicates that the smallest grid of size $N_x \times N_y = 1340 \times 400$ is sufficient to accurately resolve the growth rate and frequency of the bubble modes. This can be justified by noticing that these structures are rather large in size, resulting in an easily achievable constraint for resolving the disturbance length scale. This latter point is discussed next, as the results of a grid convergence analysis for the resolvent analysis of shorter wavelength convective instabilities are shown in Fig. 2b.

The influence of the streamwise mesh resolution on the optimal gain value for the dominant second mode is assessed by choosing the second mode optimal gain as a convergence metric, since the second mode disturbances represent the linear instability with the shortest streamwise wavelength in this flow. Starting from a mesh of size $N_x \times N_y = 1760 \times 550$, the streamwise resolution of the mesh is increased successively until the second mode gain reaches convergence. For this, $N_{x,tip} = 150$ and $N_{x,cyl}$ is augmented to make the total number of streamwise points reach $N_x \approx 5000$. Additionally, a wall-normal grid resolution $N_y = 550$ was found to be sufficient to accurately resolve the convective structures. Figure 2b highlights the substantial sensitivity of the optimal gain value to the streamwise grid resolution for two frequencies. For the initial grid size $N_x = 1760$, the second-mode peak is not visible on the gain map. A grid resolution of at least $N_x = 2500$ points is necessary to obtain less than 10% error on the gain value for $f = 220$ kHz. This grid requirement is even more restrictive for instabilities at $f = 225$ kHz, where the error remains around 15% for $N_x = 2500$. These trends are directly related to the cut-off spatial resolution of the considered numerical schemes for the differential operators. The 7th-order schemes used for the computation of the Jacobian entries have a dissipation cut-off of around 7 points per wavelength. Hence, any energy content at finer scales will not be fully resolved. This explains the stringent grid requirement for capturing instabilities at higher frequencies, which exhibit shorter streamwise wavelengths. The grid requirements explored in this section will ensure a properly converged baseflow for the comparisons made in the following section.

C. Baseflow comparisons between NASA/ONERA-CEA on CCF12

Solutions are computed for four flow conditions corresponding to sharp and blunt nosetip experiments performed in the R2Ch and BAM6QT wind tunnels (see companion paper [14]). In what follows, only the baseflow for the sharp geometry are compared. The blunt baseflows comparison will be presented in future studies. The flow parameters are

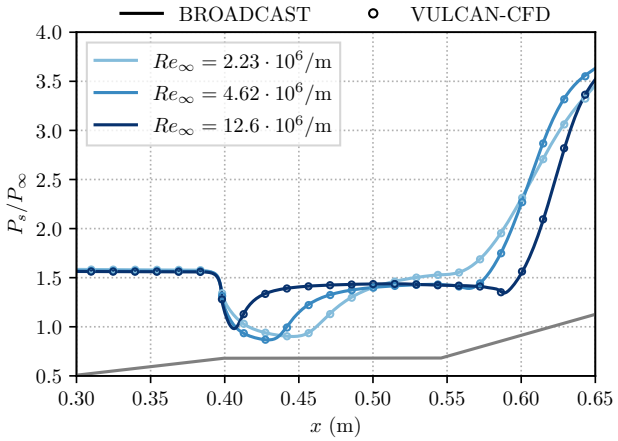

(a) Streamwise evolution of the normalized wall pressure for different Reynolds numbers. The solid lines correspond to the BROADCAST solutions while solid circles to the VULCAN-CFD ones.

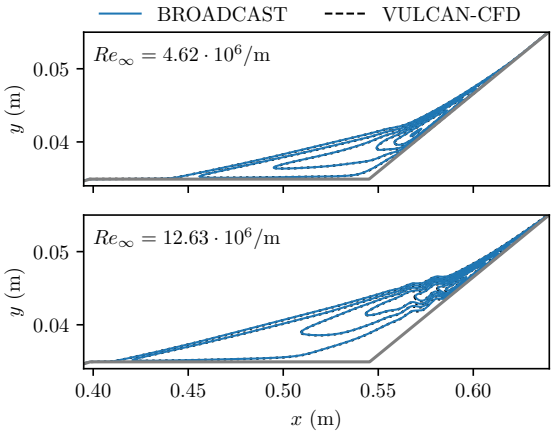

(b) Bubble topology at $Re_\infty = 4.62$ $\mathbf{m^{-1}}$ and $Re_\infty = 12.63$ $\mathbf{m^{-1}}$, flare angle is exaggerated for readability.

Fig. 3 Baseflow comparisons between BROADCAST and VULCAN-CFD.

given in Tab. 3 alongside conditions for the $Re_\infty = 12.63 \times 10^6$ m^{-1} case previously explored by [35]

Table 3 Computational flow conditions.

Facility	$Re_\infty \times 10^6$ (m^{-1})	R_n (mm)	u_∞ (m/s)	ρ_∞ (kg/m^3)	T_∞ (K)	T_0 (K)	T_{wall} (K)	P_0 (kPa)
R2Ch	2.229	0.1	907.92	0.00920	56.977	467.21	300	237.50
R2Ch	4.614	0.1	990.41	0.02128	67.800	555.96	300	653.90
BAM6QT	12.63	0.1	854.10	0.04801	50.422	413.46	300	1097.09
R2Ch	9.870	5	1033.65	0.04795	73.850	605.57	300	1605.00

From the aforementioned grid requirements, BROADCAST computations were made on grid resolutions of $N_x \geq 4300$ and $N_y = 550$, ensuring an optimal gain error below 1% for the considered instabilities, while VULCAN-CFD computations are performed on a grid of $N_x \times N_y = 3601 \times 1201$ points. The different grid sizes and meshing techniques used provide a strong validation between stability results and show consistency in the implementation of the numerical methods across institutions. We used the built-in capability in VULCAN-CFD to iteratively adapt the computational grid to the bow shock, the boundary layer, and the re-attachment shock [36]. The adaptation process ensures that enough points are clustered next to the model surface to resolve the thickness of the boundary layer within the separation region, as well as aligning the grid to the shocks. For the adaptation process, the boundary layer edge is defined as the wall-normal position where $h_0/h_{0,\infty} = 0.99$, with h_0 denoting the total enthalpy, i.e., $h_0 = h + 0.5(\bar{u}^2 + \bar{v}^2 + \bar{w}^2)$, where $h = c_p \bar{T}$ is the static enthalpy. An offset is also applied and ensures the chosen number of cells in the wall normal direction will properly resolve the entropy layer as well. For both solvers, Sutherland's law for air is used to calculate the dynamic viscosity as a function of temperature, and the isothermal wall with $T_w^* = 300$ K was used alongside the freestream conditions listed in Tab. 3.

The laminar flow over a cone-cylinder-flare geometry at the selected conditions contains a separated region at the cylinder-flare junction. The topology of the separation bubble is sensitive to both the resolution of the boundary layer gradients and the associated separation and reattachment shocks. In Fig. 3a, the predicted wall pressure distributions are compared within the separation region at three different Reynolds numbers. Both solvers show an excellent agreement in regard to the surface-pressure trends at all Reynolds numbers, with the VULCAN-CFD results shown as filled circles perfectly superimposed to the BROADCAST solutions shown as solid lines. Additionally, Fig. 3b shows the bubble topology for the sharp nosetip at $Re_\infty = 4.62 \times 10^6$ m^{-1} and $Re_\infty = 12.6 \times 10^6$ m^{-1}, with 15 iso-contours of streamwise

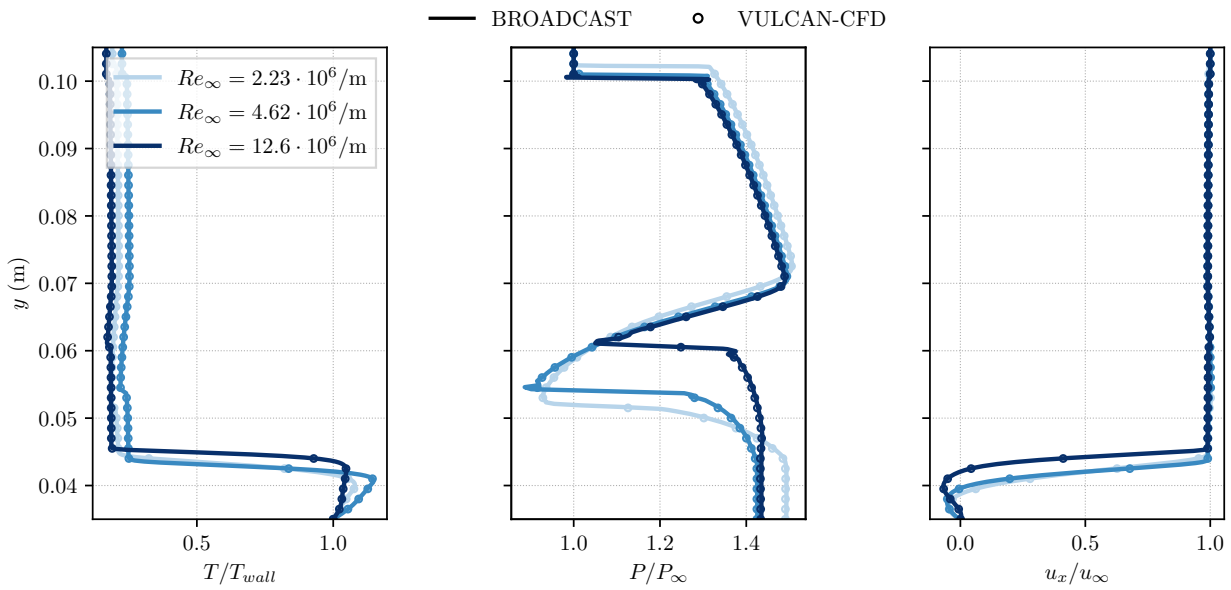

Fig. 4 Wall-normal profiles of the normalized temperature, pressure, and streamwise velocity at the cylinder-flare junction. [26].

velocity for $u_x \in [-280, 20[$ m/s drawn for both computations. At these flow conditions, the laminar separation bubble is large and both solutions show perfect agreement.

Finally, Fig. 4 presents profiles of non-dimensional temperature (T/T_{wall}), pressure (P/P_∞), and streamwise velocity (u_x/u_∞) for all three sharp cases at the cylinder-flare junction. Perfect agreement is observed with the VULCAN-CFD solution entirely overlapping the BROADCAST solution. Although not shown here for conciseness, a similar agreement is seen for the wall-normal derivative of these variables.

These comparisons confirm the capability of both numerical methods to obtain consistent results across different Reynolds numbers for the CCF12 geometry, even for different meshes. This consistency is further demonstrated by looking at stability analyses performed on these baseflows.

V. Numerical Analysis of Linear Instabilities

The CCF12 flows are known to support convective and global instabilities within the boundary layer and the separated region. The following sections aim at exploring these linear instabilities for different Reynolds numbers and nosetip bluntness values.

A. Global stability analysis

The global stability of the CCF12 baseflows for a sharp nosetip at $Re_\infty = 2.23 \times 10^6$ m^{-1} and $Re_\infty = 4.62 \times 10^6$ m^{-1} is investigated with two different codes for baseflows obtained from the two solvers. The eigenvalue problem (EVP) stated in Eq. 3 is solved by casting it in a shift-and-invert form to look for the N_λ closest eigenvalues to a target λ_t in the complex plane. The obtained EVP is solved using a Krylov-Schur algorithm [37].

The eigenvalue spectra are given in Fig. 5 with the complex plane (ω, σ) on the left and the growth rate-azimuthal wavenumber plane (σ, m) on the right. The solutions from the eigenvalue solvers are superimposed on the right plot with dots and circles with black edges, respectively. A point-to-point agreement is found for both Reynolds numbers for the leading eigenvalues. This shows that both eigenvalue solvers converged to the same instabilities.

As the Reynolds number increases from $Re_\infty = 2.23 \times 10^6$ m^{-1} to $Re_\infty = 4.62 \times 10^6$ m^{-1}, the right plot shows the bifurcation of the leading mode from a stable state (blue branches) to an unstable state (red branches) with a leading three-dimensional instability at $m = 5$. This bifurcation corresponds to an eigenvalue crossing the imaginary axis at $\omega = 0$, leading to a three-dimensionalization of the baseflow. Similar behavior was shown for first bifurcations in blunt and sharp flows for the CCF12 and CCF10 geometries [4, 5]. At $Re_\infty = 4.62 \times 10^6$ m^{-1}, a secondary branch of unsteady

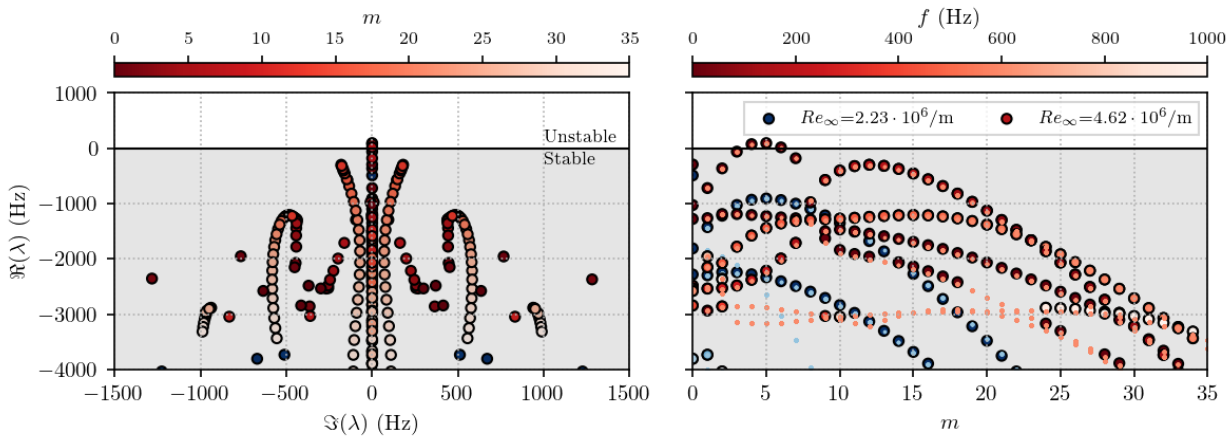

Fig. 5 Leading eigenvalues associated with the global modes for the CCF-R01 configuration. The left plot shows them in the complex plane with the color corresponding to the azimuthal wavenumber m, while the right one shows the growth rate as a function of the wavenumber.

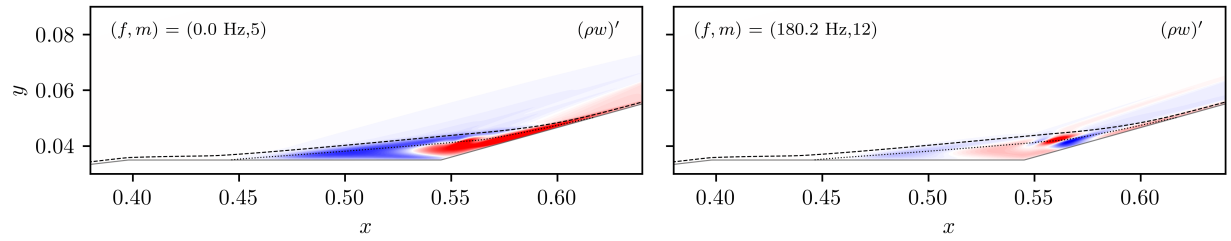

Fig. 6 Leading global modes for case Re= 4.62×10^6 $\mathbf{m^{-1}}$. Left mode corresponds to the leading unstable eigenvalue seen in Fig. 5-right. The right mode corresponds to the leading mode of the stable branch closest to the instability threshold

modes is also seen in the vicinity of the instability threshold around $m = 12$. Modes from these two branches are shown in Fig. 6 for the transverse momentum disturbance field $(\rho w)'$. The $(f, m) = (0\text{ Hz}, 5)$ mode is a three-dimensional bubble instability with amplitude spanning the entirety of the separated region. In contrast, the $(f, m) = (1132\text{ Hz}, 12)$ mode is concentrated near the reattachment region with some low disturbance amplitude throughout the separation region. Both modes exhibit characteristics similar to global modes observed in various hypersonic shock-boundary layer configurations, including oblique shock boundary layer interactions [7] and hollow cylinder-flare compression ramps [8]. Such global modes may lead to a three-dimensional and unsteady flow upon which the convective instabilities studied in the next section can evolve.

B. Convective instabilities over CCF12

For the following two sections, the convective instabilities obtained with the resolvent analysis by ONERA/CEA are compared to those obtained by NASA using the hybrid PSE and HLNSE approach. A first evaluation of the flow amplification peaks obtained with the Resolvent is given for the three Reynolds numbers on the sharp case. Then the amplification map of the blunt case obtained from the nonmodal optimization performed within the NASA framework is discussed.

Figure 7 shows the optimal gain map for the sharp cone for different Reynolds numbers. On these maps, the amplification is presented in the frequency-azimuthal wavenumber domain, allowing us to obtain an understanding of the dominant linear mechanisms. Three dominating mechanisms are found in the flow. These mechanisms can be listed as steady streamwise waves corresponding to streaks; unsteady oblique waves at frequencies mostly under 100 kHz corresponding to first Mack mode waves; unsteady planar waves at higher frequencies ($\geq$ 110 kHz) corresponding to

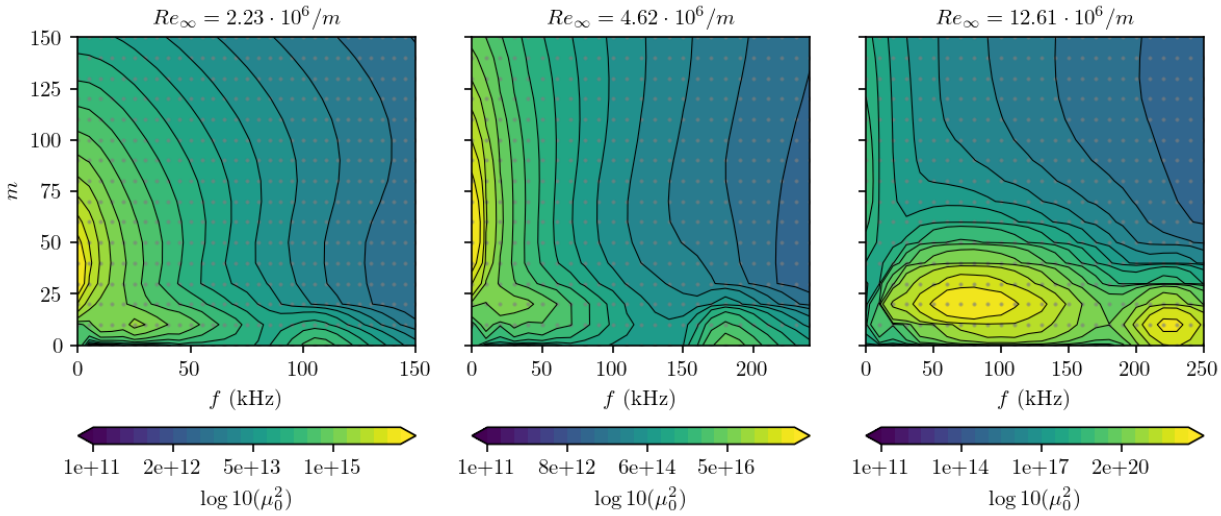

Fig. 7 Optimal gain map in frequency f and wavenumber m space obtained from Resolvent analysis with the ONERA/CEA framework.

second Mack mode instabilities. The optimal modes shape corresponding to those two most linearly amplified unsteady mechanisms at these Reynolds numbers are reported in Fig. 8.

The azimuthal-wavenumber and frequency evolution of these modes with Reynolds number show interesting trends. Stationary streaks represent the most amplified disturbance mechanism along the entire geometry for the lower Reynolds cases $Re_\infty = 2.23 \times 10^6$ m^{-1} and $Re_\infty = 4.62 \times 10^6$ m^{-1}, and their peak amplification factors are at least one order of magnitude larger than those of the unsteady waves. The maximum response amplitude occurs on the flare of the model in the vicinity of the reattachment point. These disturbances also exhibit an increasing azimuthal wavenumber for peak amplification as the Reynolds number is increased, which is consistent with the thinning of the boundary layer, and agrees with the previously reported trends in optimal streak characteristics as a function of the Reynolds number [38]. On the other hand, the optimal gain of the unsteady modes increases steadily with the Reynolds number and they become the dominant linear mechanism at $Re_\infty = 12.63 \times 10^6$ m^{-1}, with a gain of five orders of magnitude higher than the streaks. The optimal first-mode instability displays a frequency increase from about 25 kHz to 80 kHz between $Re_\infty = 2.23 \times 10^6$ m^{-1} and $Re_\infty = 12.63 \times 10^6$ m^{-1}. This amplification peak also broadens with the Reynolds number with substantially amplified frequencies at $Re_\infty = 12.63 \times 10^6$ being in $f \in [50, 110]$ kHz. A slight increase in the azimuthal wavenumber is also observed as the optimal gain peak moves from $m \approx 10$ to $m \approx 20$ with the Re_∞ increase. The second-mode waves also present a clear shift to increasing frequency, with the frequency of peak amplification moving from $f = 110$ kHz at $Re_\infty = 2.23 \times 10^6$ m^{-1} to $f = 225$ kHz at $Re_\infty = 12.63 \times 10^6$ m^{-1}. This is consistent with the well-known scaling for second-mode frequency, $f \propto u_e/2\delta_{99}$. A more interesting behavior is found by looking at the optimal azimuthal wavenumber. At the lower Reynolds number, the second-mode instability is most amplified for planar waves with $m = 0$ which is consistent with the previous results issued from locally parallel stability theory [39]. However, as the Reynolds number is increased to $Re_\infty = 12.63 \times 10^6$ m^{-1}, the maximal amplification of this instability is found for $m = 10$ showing that the most amplified second-mode instabilities are now slightly oblique waves. The reason for this shift in azimuthal wavenumber is not yet explained and remains to be investigated in future studies.

To complement the optimal gain maps shown in Fig. 7 for the sharp nosetip, the optimal responses associated with the first-mode and second-mode amplification peaks at selected (f, m) are presented in Fig. 8 for the streamwise momentum disturbance field. In relation to the convergence shown in Fig. 2b, the increase in streamwise wavenumber with the Reynolds number can be qualitatively observed with the reduction of the size of the coherent structure along the boundary layer edge. Additionally, for the first- and second-mode waves, radiation outside the viscous region are observed. Similar radiation outside the boundary layer was also observed in SPOD modes at similar Reynolds numbers along the shear layer [14]. This link with other recent experimental observations is further discussed in the next section.

The nonmodal growth of instabilities for the blunt nose case with $R_n = 5$ mm at $Re_\infty = 9.87 \times 10^6$ m^{-1} is studied using the NASA framework as defined in Sec. III.D. The HLNSE are used to compute the optimal disturbance energy gain over the interval from $\xi_0 = 0.05$ m to $\xi_1 = 0.643$ m. The initial location was selected based on (i) calculations

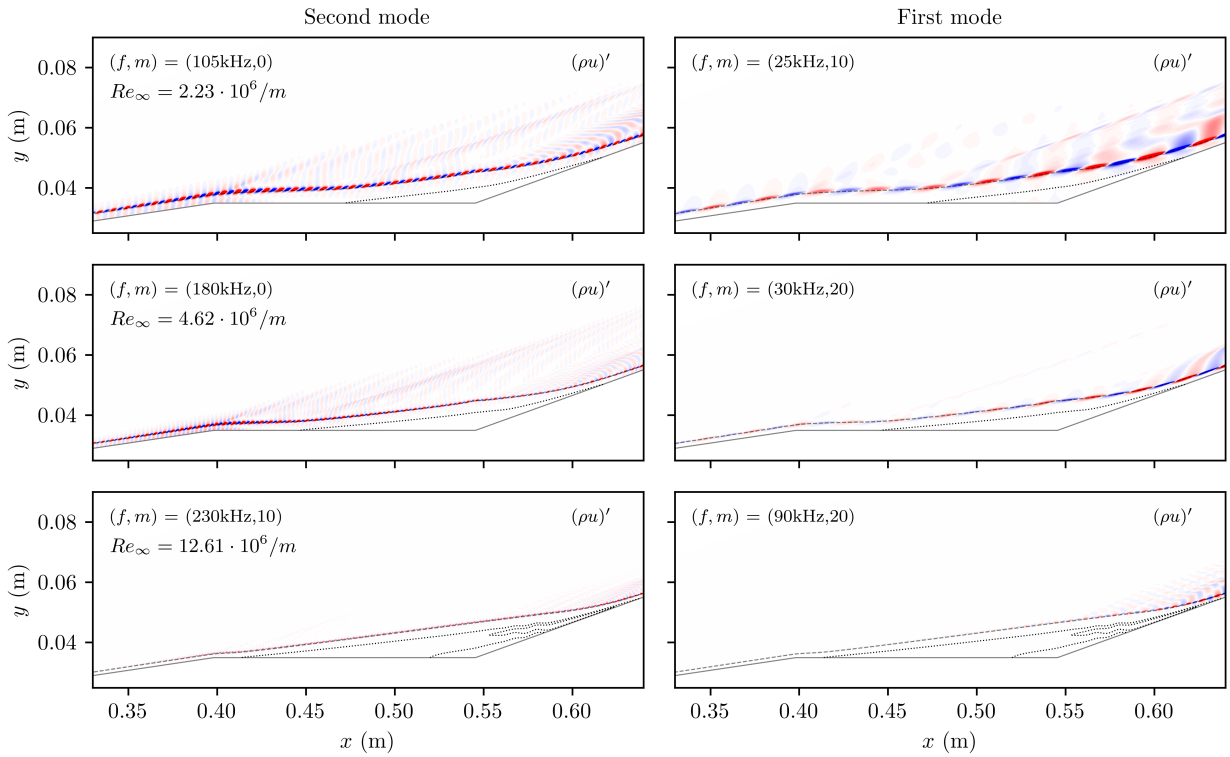

Fig. 8 Streamwise momentum perturbation contours for the second- and first-modes (left and right columns) at different freestream Reynolds numbers.

with different initial locations that showed a minimal change in disturbance amplification when the inflow location was shifted further upstream, and (ii) to allow for the decay of perturbations far from the wall and below the bow shock. The outflow location was selected to approximately coincide with the location of the last PCB sensor in the experiments.

A frequency-azimuthal wavenumber map of the amplification of the instabilities is presented in Fig. 9a, along with a colormap of N-factor evolution based on Chu's energy norm along the length of the CCF configuration. The most amplified disturbance corresponds to a steady perturbation related to the streamwise streaks with $m = 55$. The eigenfunction corresponding to this peak amplification is shown in Fig. 9b-top. It may be observed that the streak achieves its maximum amplitude after the reattachment point, similar to the findings for the sharp geometry. The most amplified unsteady instability is a planar disturbance of frequency of $f = 15$ kHz, with a peak N-factor that is nearly twice as small in comparison with the N-factor for the stationary streaks. The corresponding eigenfunction is shown at the bottom of Fig. 9b. The temperature disturbance seems to peak at the top of the separation bubble, within elongated structures along the shear layer at the top of this bubble. This mode shape is reminiscent of the schlieren SPOD modes obtained at the same Reynolds number, albeit for a slightly higher frequency, in Ref. [14].

The above unsteady waves have not been fully characterized as yet and will require further analysis. It should be noted that no higher frequency waves are found to be substantially amplified for this baseflow, suggesting that second-mode waves observed in the sharp case are completely stabilized by the effects of the blunt nosetip. This result is consistent with the previous findings indicating that the presence of the entropy layer suppresses the first- and second-mode disturbances [16, 40].

Having mapped the leading linear instability mechanisms supported by the baseflows of interest for the sharp and blunt configurations, the following section outlines the findings of a preliminary study that seeks to provide further understanding of the nature of waves found to undergo peak amplification along the separated region.

C. Local instability investigation

To understand the fundamental mechanisms driving the instabilities of the recirculation bubble, a LST investigation was conducted using the JoKHeR stability package [41–45]. A profile in the separated region just upstream of the

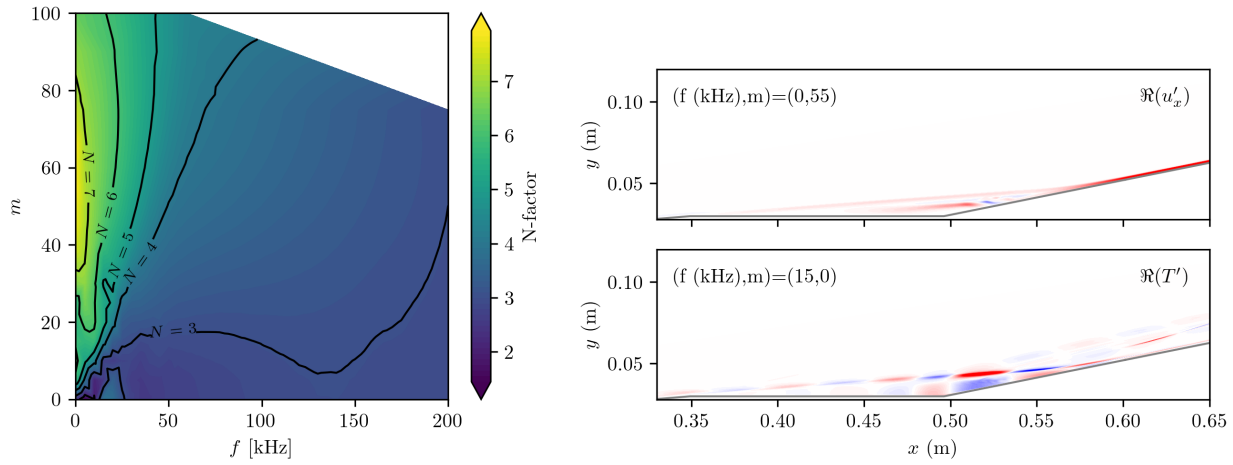

(a) N-factor map computed from the nonmodal analysis. **(b) Modes at the two leading amplification peaks**

Fig. 9 Results from the nonmodal analysis using HNLSE for CCF12 with $R_n = 5$ mm at $Re_\infty = 9.87 \times 10^6$ m^{-1}.

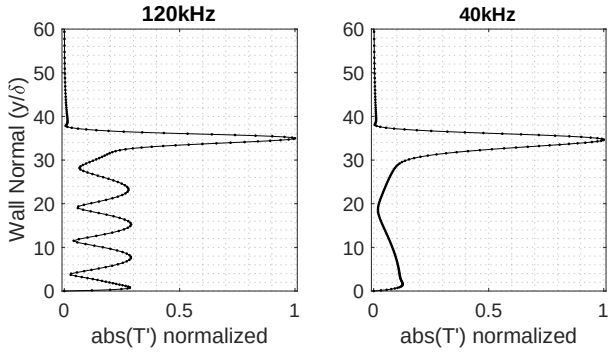

Fig. 10 Perturbation temperature (normalized) eigen-mode structure of the 120kHz (left) and 40kHz (right) instability modes over the cylinder.

cylinder-flare junction was considered and two independent unstable modes (related to the previously discussed modes that were identified as first and second mode) were identified (figure 10). Further, a study of the energy budgets was conducted under the assumption of inviscid flow dynamics. Following [46], disturbance energy of the form

$$\underbrace{\frac{\bar{\rho}}{2}\frac{\bar{D}\langle\vec{u'}^2\rangle}{Dt} + \frac{\gamma M^2}{2\bar{\rho}c^2}\frac{\bar{D}\langle\vec{P'}^2\rangle}{Dt}}_{\text{dist. energy}} = \underbrace{\langle -\bar{\rho}u'v'\frac{\partial\bar{U}}{dy} - \bar{\rho}v'w'\frac{\partial\bar{W}}{dy}}_{\text{velocity advective}} \underbrace{- \left(\vec{u'}\cdot\vec{\nabla}\right)p' - \gamma M^2 P'\left(\vec{\nabla}\cdot\vec{u'}\right)}_{div.\ acst.\ pwr}\rangle. \tag{9}$$

was considered. It should be noted that this energy norm is consistent with the energy norm used in the analysis of compressible turbulence [47]. It is also very similar to the Chu energy norm [48], if pressure is expanded into density and temperature perturbation quantities, which is very popular in optimal growth studies [49]. Note, figure legends have been labeled as follows: UV indicates traditional Reynolds Stress $-\bar{\rho}u'v'\frac{\partial\bar{U}}{dy}$. UDxP, VDyP and WDzP indicate the components of $-\left(\vec{u'}\cdot\vec{\nabla}\right)p'$. PDxU, PDyV and PDzW indicate the components of $-\gamma M^2 P'\left(\vec{\nabla}\cdot\vec{u'}\right)$. All DAP indicates the profile of all the divergence of acoustic power terms with positive indicating an energy source.

Figure 10 provides clues as to the instability mechanism for each of the unstable modes. Notice that the 120kHz mode exhibits a high-order resonant type structure, similar to that observed for Mack's second-mode instability, and that

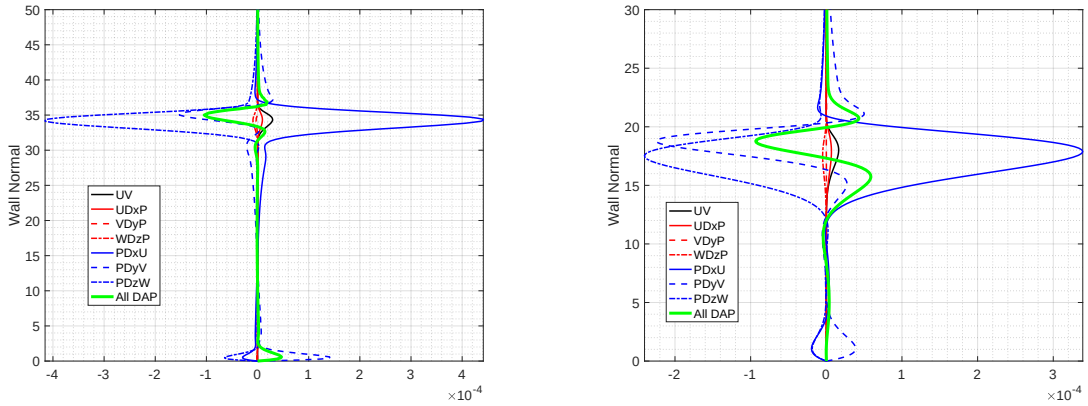

Fig. 11 Left: Inviscid energetics of the 40kHz instability over the cylinder. Right: Inviscid energetics of a $M_\infty = 6$, self-similar boundary layer first-mode instability.

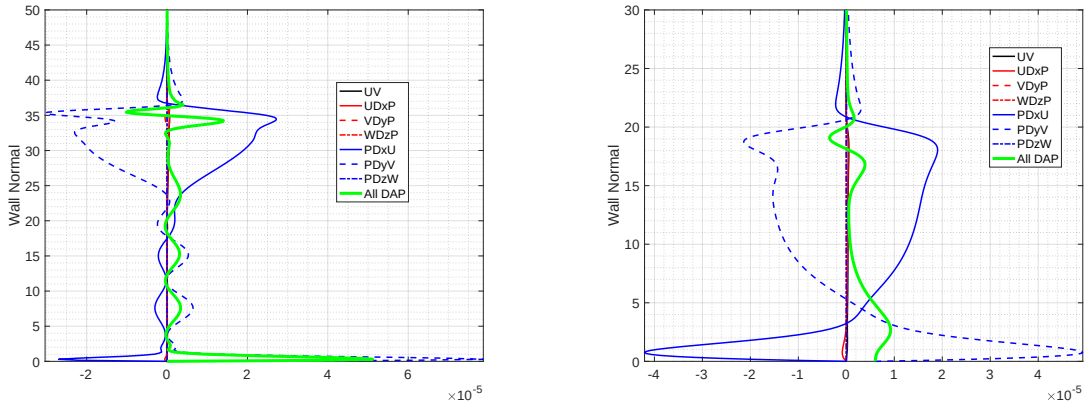

Fig. 12 Left: Inviscid energetics of the 120kHz instability over the cylinder. Right: Inviscid energetics of a Mach = 6, self-similar boundary layer second-mode instability.

the 40kHz mode exhibits a strong signal at the shear layer, similar to that observed for Mack's first-mode instability. Further comparing the inviscid energetics of the 40kHz mode to the energetics of a $M_\infty = 6$, self-similar boundary layer Mack's first-mode, it is observed that both disturbances have a very similar energetics signature (Fig. 11). Likewise, a similar energetics signature is observed when considering a comparison between the inviscid energetics of the 120kHz mode and that of Mack's second-mode disturbances in a $M_\infty = 6$, self-similar boundary layer (Fig. 12).

These findings tentatively suggest that there are at least two fundamental instability mechanisms present in the recirculation bubble. The lower frequency instability is concentrated near the shear layer and behaves in a very similar manner to Mack's first-mode instabilities. The higher frequency instability exhibits a resonant structure that is similar to the resonant structure of Mack's second-mode disturbances, and thus, suggests a thermoacoustic resonance mechanism [50] (though of higher order, perhaps a fourth modeaccording to Mack's classification).

VI. Comparison of Computed and Experimentally Measured Convective Instabilities

Transitional boundary layer data obtained from experimental campaigns in three different wind tunnels are compared to the linear dynamics computed with the Resolvent and PSE/HNLSE introduced above. The experimental dataset used for comparison corresponds to the measurements of high-frequency pressure disturbances at the wall as obtained from piezoelectric pressure transducers (PCB sensors). For the numerical data, the pressure disturbance field is considered

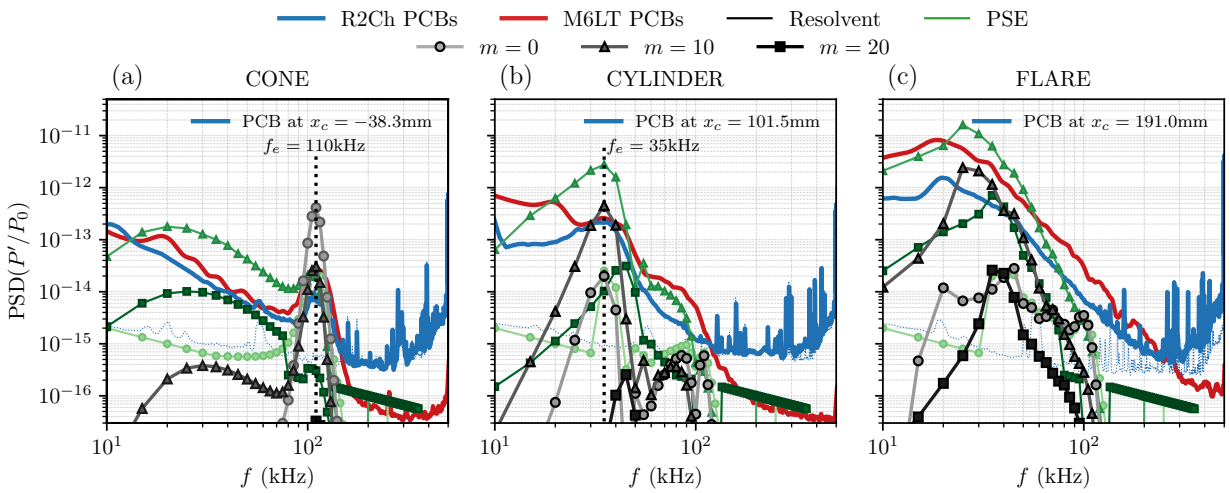

Fig. 13 Comparison of PCB measurements at M6LT and R2Ch wind tunnels against numerical spectra computed at the same locations from Resolvent modes and from PSE/HNLSE analysis for CCF12-R01. The sensors coordinate are taken from the cone-cylinder junction.

for the modes computed by the resolvent analysis and the PSE/HNLSE. The local amplitude of the pressure field based on the eigenfunctions is extracted at the sensor position, allowing us to predict the wall pressure spectra based on the instability calculations. The actual numerical sensor locations are selected based on the PCB positions in the experiments at M6LT, R2Ch, and the BAM6QT as described in Ref. [14].

A. Comparison with conventional wind-tunnel data

First, we compare the predicted spectra with the experimental measurements in the two conventional wind tunnels. To ensure a meaningful comparison of the disturbance dynamics, due care was taken to establish that the computed baseflows were as close as possible to those in the experiments. The experimental Reynolds number is chosen to be $Re_\infty = 2.23 \times 10^6$ m^{-1}. In the experiments, these conditions were considered to offer a laminar flow topology, therefore limiting the possible mean-flow effect in the comparison against the numerical laminar baseflows. Furthermore, the global stability analysis presented in Fig. 5 indicated that, for these conditions, the baseflow is also globally stable, meaning that the dynamics of measured disturbances should be confined to convective instabilities.

Figure 13 shows the comparison with the experimental spectra in M6LT and R2Ch for three PCB sensors at the end of the cone, the cylinder, and the flare, respectively. The resolvent spectrum is presented in shades of gray and the PSE/HNLSE spectrum is in shades of green. For these two numerical datasets, spectra are presented at three different wavenumbers as the peak amplification at different frequencies can be related to the waves propagating at different orientations, such as that in Fig. 7. In contrast, the experimental spectrum depicts the superposition of instabilities at all wavenumbers for a given frequency.

To enable a comparison between the measured spectra of disturbance amplitudes and the predicted spectra of amplification ratios, we set the amplitude of the predicted linear modes to match the experimental data at a reference location. In particular, this amplitude was chosen such that the second-mode disturbance at $m = 10$ and $f = 110$ kHz matches the amplitude of the peak at $f = 110$ kHz from the measured spectrum in the M6LT. This initial amplitude is applied to all frequencies at that point and the predicted spectra at the downstream stations only account for the growth of the instabilities based on this initial amplitude.

Overall, the computed and measured spectra at the three stations of interest (Fig. 13) show reasonably good agreement in regard to the streamwise evolution of the disturbance amplitudes. The computed growth of the shear-layer modes and the strong amplification of the low-frequency peaks captures the experimentally observed trends. On the cone, there is excellent agreement between the peak second-mode frequency in the experiment ($f = 110$ kHz) and the predictions of both the resolvent and the PSE/HNLSE frameworks. However, there is a notable discrepancy in the peak amplitude across different wavenumbers. The resolvent modes show a clear separation between wavenumbers, whereas the PSE/HNLSE shows similar amplitudes for $m = 0$ and $m = 10$. Following the computed amplitude evolution on the

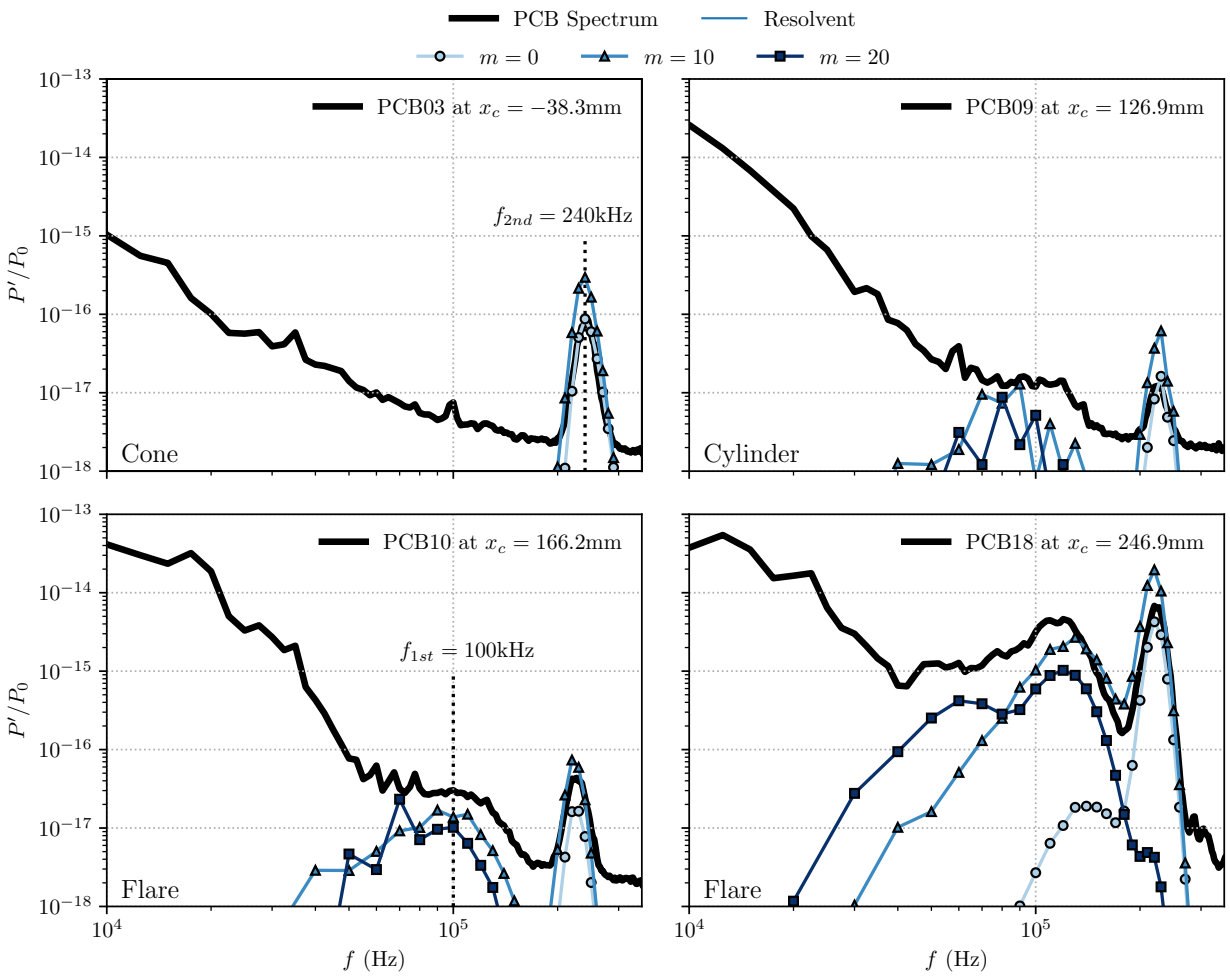

Fig. 14 Comparison of the experimental PCB spectra at $Re_\infty = 12.1 \times 10^6$ m^{-1} with the numerical ones at the same location obtained from linear optimal Resolvent modes at $Re_\infty = 12.6 \times 10^6$ m^{-1} . Numerical mode amplitudes are scaled to the second mode peak for PCB03 at $m = 0$.

cylinder, both frameworks are again able to make accurate predictions of the peak frequency of the first-mode instabilities, measured at $f = 35$ kHz in the experiment. The amplitude match is less clear in that case as the PSE/HNLSE tends to over-predict the first-mode amplitude at $f = 35$ kHz, but seems to have a closer agreement for frequencies between 50 kHz and 100 kHz with the M6LT measurements. The resolvent mode at $m = 10$ shows a good match with the measured first mode amplitude but does not capture the same amplitude as the PSE for higher frequencies. On the flare, the PSE/HNLSE and the resolvent again showed the same peak frequency of around 25 kHz, albeit with some differences in the final peak amplitude. However, this computed peak does not match the experimental measurement for $f = 20$ kHz. This suggests that the current analysis on the axisymmetric laminar baseflow may be missing a physical mechanism associated with the flare. With the strong amplification found after the reattachment, it is possible that a secondary flow has been produced by linear and/or non-linear mechanisms and led to the amplification of lower frequencies. Differences between computed instabilities and experimental measurements are not surprising in view of the known sensitivity of laminar-turbulent transition to multiple factors associated with the flow. This is particularly evident in conventional wind tunnels, where the noisy freestream induces transitional dynamics even at lower Reynolds numbers.

B. Comparison with data from quiet wind tunnel

A comparison is also made with a quiet tunnel experiment involving the sharp nosetip model in the BAM6QT for $Re_\infty = 12.63 \times 10^6$ m^{-1}. This comparison is made for four PCB sensors that were located, respectively, at the end of the cone, on the cylinder, and two on the flare before and after the reattachment point [14]. In the quiet wind tunnel, transition was not observed at this Reynolds number, the bubble reattachment point was optically observed at $x_c = 250$ mm and is found to be $x_c = 238$ mm in the computed results. For this case, only the resolvent-based optimal modes are available and they are compared in Fig. 14. Again, the pressure disturbance amplitudes of the optimal responses are scaled by matching the peak amplitude at $f = 240$ kHz and $m = 10$ to the measured peak in the spectrum of PCB03.

A perfect agreement is found between the measured and computed second mode frequency at the end of the cone. For PCB09 on the cylinder, the frequency is well predicted and a very close match is also found for the disturbance amplitude. A lower amplitude peak associated with first-mode disturbances starts to become visible in the resolvent spectrum, but it is difficult to discern the presence of a corresponding peak in the experimental spectrum. For the PCB10 sensor along the flare, a similar agreement in peak disturbance frequency is observed for the second mode disturbances, albeit with a small discrepancy in the disturbance amplitudes. A lower frequency, broadband peak is measured for $f \approx 100$ kHz. This broadband signature is captured with the resolvent analysis for oblique modes at $m = 10$ and $m = 20$. However, the computed amplitude is found to be one order of magnitude lower than the experimental pressure disturbances corresponding to this broadband peak. Finally, we perform a similar comparison for an axial station close to the end of the flare, i.e., downstream of the reattachment point, where a strong amplification of pressure disturbance is observed in the experiment. The measured and computed peak frequencies show a perfect agreement for both first-mode and second-mode waves. A decent agreement is also observed for the peak amplitude. In particular, the second-mode amplitude is overestimated by the resolvent analysis for $m = 10$ but seems to agree well at $m = 0$. A similar observation applies to first-mode waves, with a slight overprediction of the peak amplitude for $m = 10$ and a good agreement for $m = 20$. Overall, the instability trends in regard to streamwise amplification are well predicted by the resolvent analysis at the wavenumbers considered here.

It is necessary to exercise due caution in the direct interpretation of the differences in predicted amd measured disturbance amplitudes for specific values of m. A direct inspection would suggest that the resolvent analysis can provide insights into the orientation of the dominant instability wave at a given frequency in the experimental spectrum. However, such interpretation neglects multiple factors: the wave superposition captured by the PCB sensors; potential nonlinear effects; and the potential effects of global instability. A comparison of this type is also constrained by the neglect of the receptivity phase, which is an essential step during the instability evolution. The likely influence of the receptivity process is discussed hereafter.

C. Receptivity as a source of discrepancy

Now, we discuss the receptivity process by considering the singular value decomposition of the resolvent operator, equivalent to the decomposition given in Eq. 6. From this formulation of the linear Navier-Stokes equations, the growth of any linear instability $\hat{\boldsymbol{q}}$ coming from the nonmodal flow dynamics is therefore fully described by the orthogonal bases of optimal forcings $\boldsymbol{\phi}_i$ and optimal responses $\boldsymbol{\psi}_i$ [18]. Given the input-output relation of the Resolvent operator stated in Eq. 4,

$$\hat{\boldsymbol{q}} = \boldsymbol{\mathcal{R}}(\omega, m)\hat{\boldsymbol{f}}_{real}, \tag{10}$$

Neglecting the nonlinear forcing terms of the Navier-Stokes equations, any linear disturbance in the form of an external forcing $\hat{\boldsymbol{f}}_{real}$ at a given frequency and wavenumber can be written as a linear combination of the N_r vectors of the optimal orthogonal bases for the forcings and the responses [51],

$$\hat{\boldsymbol{q}} = \sum_{i=0}^{N_r-1} \underbrace{\mu_i \langle \boldsymbol{\phi}_i, \hat{\boldsymbol{f}}_{real} \rangle_f}_{c_0} \boldsymbol{\psi}_i = \boldsymbol{\mathcal{R}}(\omega, m) \sum_{i=0}^{N_r-1} \langle \boldsymbol{\phi}_i, \hat{\boldsymbol{f}}_{real} \rangle_f \boldsymbol{\phi}_i. \tag{11}$$

A key parameter in the comparison of the numerical and experimental spectra is, therefore, the projection coefficient $c_0 = \mu_i \langle \boldsymbol{\phi}_i, \hat{\boldsymbol{f}}_{real} \rangle_f$ which accounts for the projection of the disturbances $\hat{\boldsymbol{f}}_{real}$ coming from the environment onto the basis of optimal forcings $\boldsymbol{\phi}_i$, which in turn describes the receptivity of the flow at a given frequency and wavenumber.

From this definition of the receptivity process, Eq. 11 can be rewritten for a signal constrained to the wall pressure at the PCB locations such that, for the resolvent modes at a specified pair of (ω, m) we have,

$$|p'_{num}| = \underbrace{\langle \boldsymbol{\phi}_0, \boldsymbol{\phi}_0 \rangle}_{=1} |p'_{opt}|. \tag{12}$$

On the other hand, for the experimental spectrum, the following reconstruction of the wall pressure can be defined under a linear hypothesis and by considering the superposition of N_m azimuthal wavenumber, ,

$$|p'_{real}| = \sum_{m=0}^{N_m-1} \sum_{i=0}^{N_r-1} \underbrace{\langle \boldsymbol{\phi}_i, \hat{\boldsymbol{f}}_{real} \rangle}_{\leq 1} |p'_{i,opt}|. \tag{13}$$

The difference observed in Fig. 14 is explicitly shown by the Eqs. 12 and 13, where the receptivity process has been taken into account through the forcing projection term $\langle \boldsymbol{\phi}_i, \hat{\boldsymbol{f}}_{real} \rangle$. This most likely leads to a suboptimal pressure disturbance observed by the PCB sensors, as the natural forcing $\hat{\boldsymbol{f}}_{real}$ may not project efficiently on the optimal forcing such that $\langle \phi_i, \hat{\boldsymbol{f}}_{real} \rangle \leq 1$. Whereas in the numerical simulations, corresponding to pressure signature modeled like Eq. 12, this projection is optimal by definition. Additionally, the receptivity coefficient c_0 may also be different across the relevant range of frequencies, as the particular noise spectrum in a given wind tunnel may bias the resulting disturbance field towards specific frequency bands. In contrast, $c_0 = \mu_0$ for all frequencies in the spectrum reconstructed from the resolvent optimal modes, so that there is zero bias in the receptivity toward any specific frequency range, which is statistically equivalent to a white-noise forcing of the boundary layer.

VII. Summary and Conclusions

A numerical analysis was conducted to explore the linear flow dynamics around the CCF12 geometry (i.e., cone-cylinder-flare configuration involving a 12-degree flare) at Mach number $M_\infty = 6.0$ as part of the research activities under the NATO STO Research Task Group AVT-346. This analysis aimed at cross-validating two numerical frameworks employed respectively by NASA and ONERA/CEA. The cross-validation was also extended to comparisons with the recent experimental results from both conventional and quiet wind tunnels, offering valuable insights into the dominant instabilities for four different baseflows around CCF12.

First, three different laminar baseflows for the sharp geometry with $R_n = 0.1$ mm were validated. An explicit methodology for computing the baseflow solutions is provided, and wall pressure distributions and boundary layer profiles of three different variables are compared across the two flow solvers. Both codes exhibit a perfect agreement at all three Reynolds numbers considered. Additionally, grid-convergence requirements for global stability computations on such geometries are discussed, emphasizing the necessity of ensuring sufficient spatial resolution for the accurate prediction of convective instability amplification.

Building upon these baseflows, the global stability analysis of the sharp geometry is explored, extending up to the critical Reynolds number. At approximately $Re_\infty = 4.62 \times 10^6$ m^{-1}, the flow bifurcates into a three-dimensional steady state. Eigenvalue spectra predicted via different meshes and methodologies are compared with each other at two different values of the Reynolds number. This analysis confirms the consistency of the computed physics using both methods.

Following the examination of the global spectra, we also analyzed the convective instabilities around the geometry with a sharp cone tip. Resolvent analysis for this case employed the full axial domain. On the other hand, the convective instability analysis for the CCF12 configuration with a blunt nose tip was conducted using resolvent analysis based on an inflow and an outflow plane. The analysis of the sharp geometry reveals how the nonmodal disturbance evolution varies with the Reynolds number. Steady streamwise streaks are found to dominate at low Reynolds numbers, while unsteady first- and second-mode instabilities exhibit a strong amplification at $Re_\infty = 12.63 \times 10^6$ m^{-1}. Additionally, intriguing azimuthal wavenumber trends for the second mode are observed as these waves become oblique with $m = 20$ for the highest Reynolds number. On the other hand, the analysis of the blunt nosetip geometry indicates the stabilization of first- and second-mode instabilities, while the streaks remain amplified along the flare. Another planar unsteady mechanism with a low-frequency peak is identified in the predicted disturbance spectra, which appears to correlate with the recent experimental observations in a similar flow [14]. However, further investigations are required for a comprehensive comparison with the wind tunnel measurements.

Both local linear stability theory and inviscid energy budgets are used to obtain further insights into the nature of the convective instabilities in the separation bubble of the sharp case. The inviscid analysis of the bubble eigenfunction is

compared to similar results obtained in a self-similar boundary layer, highlighting the distinct characteristics of the two fundamental instability mechanisms at low and high frequencies. The low-frequency mechanism predominantly resides in the shear layer and exhibits a behavior that is akin to a first-mode instability, while the high-frequency mechanism resembles the second-mode instability of a self-similar boundary layer. Remarkably, for this latter mechanism, the number of acoustic resonance lobes within the bubble seems to align with the fourth mode of acoustic type, based on the classification scheme described by Mack [39].

Finally, the evolution of convective instabilities computed with the resolvent analysis and the PSE/HLNSE methods is compared against experimental measurements. The measured data includes the surface pressure spectra at successive axial stations on the cone, the cylinder, and the flare, as measured in both conventional and quiet (i.e., low disturbance) wind tunnels. Pressure spectra from the computations are reconstructed and scaled to facilitate a comparison of amplification factors between numerical solutions and experimental measurements. The peak frequencies align very well across the resolvent analysis, PSE/HNLSE predictions, and the conventional/quiet wind tunnel data, providing further confidence in the ability of these tools to accurately predict the frequency of linear mechanisms in the laminar baseflows investigated in the experiments. However, noteworthy discrepancies are noted in regard to a similar comparison of the amplitude evolution between the experiments and the computations, respectively. In particular, for conventional wind tunnel data, there is an inconsistency between the amplitudes predicted by the PSE/HNLSE and the resolvent analysis. However, a closer agreement was observed between the resolvent analysis and the quiet wind tunnel measurements, specifically in the form of similar amplification trends for first- and second-mode instabilities in the experimental and numerical spectra. The discrepancies in amplitude are further discussed by restating the theoretical aspects of the receptivity process, highlighting potential sources of disparities, including the bias in wind-tunnel noise toward specific frequency bands and the imperfect projection of disturbances onto the basis of optimal-forcing vectors for the linear dynamics of the CCF12 flowfield.

In conclusion, this study offers a comprehensive examination of the dominant instabilities in hypersonic flows around the CCF12 geometry, combining both numerical and experimental approaches between this paper and the companion study [14]. The cross-validation and comparative analysis presented here contribute to a deeper understanding of the flow dynamics. These results also provide a set of reference solutions that may be used to validate numerical frameworks for the study of hypersonic boundary layer transition over complex geometries Future studies will focus on additional cross-validation and providing deeper insights into the comparison between the numerical and experimental results, especially for the blunt nosetip geometries.

Acknowledgments

Author CC would like to thank Dr. Cédric Content and Dr. Arthur Poulain for their valuable help and discussions on BROADCAST and global stability. The work of the NASA authors (MC and FL) was supported by the Hypersonic Technology Project (HTP) under the NASA Aeronautics Research Mission Directorate (ARMD). Authors AS and PP are supported by the U. S. Office of Naval Research under award number N00014-20-1-2261. Author PP is also partially supported by the HTP under the NASA ARMD and by the Air Force Office of Scientific Research under award number FA9550-20-1-0023. Computational resources supporting a portion of this work were provided by the DoD High-Performance Computing Modernization Program and the NASA LaRC K Cluster at the Langley Research Center.

References

[1] Esquieu, S., Benitez, E., Schneider, S. P., and Brazier, J.-P., "Flow and Stability Analysis of a Hypersonic Boundary Layer over an Axisymmetric Cone Cylinder Flare Configuration," *AIAA Paper*, 2019-2115, 2019. https://doi.org/10.2514/6.2019-2115.

[2] Benitez, E. K., Esquieu, S., Jewell, J. S., and Schneider, S. P., "Instability Measurements on an Axisymmetric Separation Bubble at Mach 6," *AIAA Paper*, 2020-3072, 2020. https://doi.org/10.2514/6.2020-3072.

[3] Benitez, E. K., Borg, M. P., Hill, J. L., Scholten, A., Paredes, P., and Jewell, J. S., "Measurements on a Blunt Cone-Cylinder-Flare at Mach 6," *AIAA Paper*, 2023-1245, 2023. https://doi.org/10.2514/6.2023-1245.

[4] Paredes, P., Scholten, A., Choudhari, M. M., Li, F., Benitez, E. K., and Jewell, J. S., "Boundary-Layer Instabilities Over a Cone-Cylinder-Flare Model at Mach 6," *AIAA SCITECH 2022 Forum*, American Institute of Aeronautics and Astronautics, 2022. https://doi.org/10.2514/6.2022-0600.

[5] Caillaud, C., Lugrin, M., Content, C., and Esquieu, S., "Global Stability Analysis of a Hypersonic Cone-Cylinder-Flare Geometry," *Proceedings of the 57th 3AF International Conference on Applied Aerodynamics*, Bordeaux, 2023.

[6] Cao, S., Hao, J., Klioutchnikov, I., Olivier, H., and Wen, C.-Y., "Unsteady Effects in a Hypersonic Compression Ramp Flow with Laminar Separation," *Journal of Fluid Mechanics*, Vol. 912, 2021, p. A3. https://doi.org/10.1017/jfm.2020.1093.

[7] GS, S., Dwivedi, A., Candler, G. V., and Nichols, J. W., "Onset of Three-Dimensionality in Supersonic Flow over a Slender Double Wedge," *Physical Review Fluids*, Vol. 3, No. 9, 2018, p. 093901. https://doi.org/10.1103/PhysRevFluids.3.093901.

[8] Lugrin, M., Beneddine, S., Garnier, E., and Bur, R., "Multi-Scale Study of the Transitional Shock-Wave Boundary Layer Interaction in Hypersonic Flow," *Theoretical and Computational Fluid Dynamics*, Vol. 36, No. 2, 2022, pp. 277–302. https://doi.org/10.1007/s00162-021-00595-7.

[9] Dwivedi, A., Sidharth, G., and Jovanović, M. R., "Oblique Transition in Hypersonic Double-Wedge Flow," *Journal of Fluid Mechanics*, Vol. 948, 2022, p. A37. https://doi.org/10.1017/jfm.2022.697.

[10] Lugrin, M., Beneddine, S., Leclercq, C., Garnier, E., and Bur, R., "Transition Scenario in Hypersonic Axisymmetrical Compression Ramp Flow," *Journal of Fluid Mechanics*, Vol. 907, 2021, p. A6. https://doi.org/10.1017/jfm.2020.833.

[11] Marxen, O., Iaccarino, G., and Shaqfeh, E. S. G., "Disturbance Evolution in a Mach 4.8 Boundary Layer with Two-Dimensional Roughness-Induced Separation and Shock," *Journal of Fluid Mechanics*, Vol. 648, 2010, pp. 435–469. https://doi.org/10.1017/S0022112009992758.

[12] Dwivedi, A., Sidharth, G. S., Nichols, J. W., Candler, G. V., and Jovanović, M. R., "Reattachment Streaks in Hypersonic Compression Ramp Flow: An Input–Output Analysis," *Journal of Fluid Mechanics*, Vol. 880, 2019, pp. 113–135. https://doi.org/10.1017/jfm.2019.702.

[13] Esquieu, S., Schneider, S., Benitez, E., and Brazier, J.-P., "Design of a Cone-Cylinder-Flare Configuration for Hypersonic Boundary-Layer Stability Analyses and Measurements with Attached and Separated Flows," *Proceedings of the 57th 3AF International Conference on Applied Aerodynamics*, Bordeaux, 2023.

[14] Benitez, E., Borg, M., Lugrin, M., Caillaud, C., Esquieu, S., McDaniel, Z., Jewell, J., Scholten, A., Paredes, P., Choudhari, M., and Li, F., "Separation and Transition on a Cone-Cylinder-Flare: Experimental Campaigns," *AIAA SciTech 2024 Forum*, AIAA, Orlando, FL, 2024. To be presented.

[15] Stetson, K., "Nosetip Bluntness Effects on Cone Frustum Boundary Layer Transition in Hypersonic Flow," *16th Fluid and Plasmadynamics Conference*, American Institute of Aeronautics and Astronautics, Danvers,MA,U.S.A., 1983. https://doi.org/10.2514/6.1983-1763.

[16] Jewell, J. S., Kennedy, R. E., Laurence, S. J., and Kimmel, R. L., "Transition on a Variable Bluntness 7-Degree Cone at High Reynolds Number," *AIAA Paper*, 2018-1822, 2018. https://doi.org/10.2514/6.2018-1822.

[17] Cao, S., Hao, J., Klioutchnikov, I., Olivier, H., Heufer, A., and Wen, C.-Y., "Leading-Edge Bluntness Effects on Hypersonic Three-Dimensional Flows over a Compression Ramp," *Journal of Fluid Mechanics*, Vol. 923, 2021. https://doi.org/10.1017/jfm.2021.552.

[18] Sipp, D., Marquet, O., Meliga, P., and Barbagallo, A., "Dynamics and Control of Global Instabilities in Open-Flows: A Linearized Approach," *Applied Mechanics Reviews*, Vol. 63, No. 3, 2010, p. 030801. https://doi.org/10.1115/1.4001478.

[19] Poulain, A., Content, C., Sipp, D., Rigas, G., and Garnier, E., "BROADCAST: A High-Order Compressible CFD Toolbox for Stability and Sensitivity Using Algorithmic Differentiation," *Computer Physics Communications*, Vol. 283, 2023, p. 108557. https://doi.org/10.1016/j.cpc.2022.108557.

[20] Sciacovelli, L., Passiatore, D., Cinnella, P., and Pascazio, G., "Assessment of a High-Order Shock-Capturing Central-Difference Scheme for Hypersonic Turbulent Flow Simulations," *Computers & Fluids*, Vol. 230, 2021, p. 105134. https://doi.org/10.1016/j.compfluid.2021.105134.

[21] Hascoet, L., and Pascual, V., "The Tapenade automatic differentiation tool: principles, model, and specification," *ACM Transactions on Mathematical Software (TOMS)*, Vol. 39, No. 3, 2013, pp. 1–43.

[22] Schmid, P. J., "Nonmodal Stability Theory," *Annual Review of Fluid Mechanics*, Vol. 39, No. 1, 2007, pp. 129–162. https://doi.org/10.1146/annurev.fluid.38.050304.092139.

[23] Chu, B.-T., "On the Energy Transfer to Small Disturbances in Fluid Flow (Part I)," *Acta Mechanica*, Vol. 1, No. 3, 1965, pp. 215–234. https://doi.org/10.1007/BF01387235.

[24] Herbert, T., "Parabolized Stability Equations," *Annual Review of Fluid Mechanics*, Vol. 29, No. 1, 1997, pp. 245–283. https://doi.org/10.1146/annurev.fluid.29.1.245.

[25] Paredes, P., Choudhari, M. M., Li, F., Jewell, J. S., Kimmel, R. L., Marineau, E. C., and Grossir, G., "Nose-Tip Bluntness Effects on Transition at Hypersonic Speeds," *Journal of Spacecraft and Rockets*, Vol. 56, No. 2, 2019, pp. 369–387. https://doi.org/10.2514/1.A34277.

[26] Paredes, P., Scholten, A., Choudhari, M. M., Li, F., Benitez, E. K., and Jewell, J. S., "Boundary-Layer Instabilities over a Cone–Cylinder–Flare Model at Mach 6," *AIAA Journal*, Vol. 60, No. 10, 2022, pp. 5652–5661. https://doi.org/10.2514/1.J061829.

[27] Andersson, P., Berggren, M., and Henningson, D. S., "Optimal Disturbances and Bypass Transition in Boundary Layers," *Physics of Fluids*, Vol. 11, No. 1, 1999, pp. 134–150. https://doi.org/10.1063/1.869908.

[28] Luchini, P., "Reynolds-Number-Independent Instability of the Boundary Layer over a Flat Surface: Optimal Perturbations," *Journal of Fluid Mechanics*, Vol. 404, 2000, pp. 289–309. https://doi.org/10.1017/S0022112099007259.

[29] Paredes, P., Choudhari, M. M., Li, F., and Chang, C.-L., "Optimal Growth in Hypersonic Boundary Layers," *AIAA Journal*, Vol. 54, No. 10, 2016, pp. 3050–3061. https://doi.org/10.2514/1.J054912.

[30] Crivellini, A., and Bassi, F., "An Implicit Matrix-Free Discontinuous Galerkin Solver for Viscous and Turbulent Aerodynamic Simulations," *Computers & Fluids*, Vol. 50, No. 1, 2011, pp. 81–93. https://doi.org/10.1016/j.compfluid.2011.06.020.

[31] Litton, D., Edwards, J., and White, J., "Algorithmic Enhancements to the VULCAN Navier-Stokes Solver," 16th AIAA Computational Fluid Dynamics Conference, June 2003. https://doi.org/10.2514/6.2003-3979.

[32] Baurle, R., White, J., Drozda, T., and Norris, A., "VULCAN-CFD Theory Manual: Ver. 7.1.0," NASA TM-2020-5000766, 2020.

[33] Baurle, R., White, J., Drozda, T., and Norris, A., "VULCAN-CFD User Manual: Ver. 7.1.0," NASA TM-2020-5000767, 2020.

[34] Li, F., Choudhari, M. M., Paredes, P., and Scholten, A., "Nonlinear Evolution of Instabilities in a Laminar Separation Bubble at Hypersonic Mach Number," *AIAA Paper*, 2022-3855, 2022. https://doi.org/10.2514/6.2022-3855.

[35] Benitez, E. K., Borg, M. P., Scholten, A., Paredes, P., McDaniel, Z., and Jewell, J. S., "Instability and Transition Onset Downstream of a Laminar Separation Bubble at Mach 6," *Journal of Fluid Mechanics*, Vol. 969, 2023, p. A11. https://doi.org/10.1017/jfm.2023.533.

[36] Scholten, A., Paredes, P., Li, F., White, J., Baurle, R., and Choudhari, M., "Automatic Boundary-Layer Adaptation of Structured Grids in VULCAN-CFD," ICCFD11 Paper 2022-1304, 2022.

[37] Stewart, G. W., "A Krylov–Schur Algorithm for Large Eigenproblems," *SIAM Journal on Matrix Analysis and Applications*, Vol. 23, No. 3, 2002, pp. 601–614. https://doi.org/10.1137/S0895479800371529.

[38] Hanifi, A., Schmid, P. J., and Henningson, D. S., "Transient Growth in Compressible Boundary Layer Flow," *Physics of Fluids*, Vol. 8, No. 3, 1996, pp. 826–837. https://doi.org/10.1063/1.868864.

[39] Mack, L. M., and Reshotko, E., "Boundary-Layer Linear Stability Theory," 1984, p. 84.

[40] Kennedy, R. E., Jewell, J. S., Paredes, P., and Laurence, S. J., "Characterization of Instability Mechanisms on Sharp and Blunt Slender Cones at Mach 6," *Journal of Fluid Mechanics*, Vol. 936, 2022, p. A39. https://doi.org/10.1017/jfm.2022.39.

[41] Kuehl, J. J., Perez, E., and Reed, H. L., "JoKHeR: NPSE Simulations of Hypersonic Cross Instability," 2012. https://doi.org/10.2514/6.2012-921.

[42] Kuehl, J. J., "Discrete- and finite-bandwidth-frequency distributions in nonlinear stability applications," *Physics of Fluids*, Vol. 29, No. 2, 2017. https://doi.org/10.1063/1.4975158.

[43] Batista, A., and Kuehl, J. J., "Local wall temperature effects on the second-mode instability," *Journal of Spacecraft and Rockets*, Vol. 57, No. 3, 2020, pp. 580–595. https://doi.org/10.2514/1.A34620.

[44] Khan, A. A., Liang, T., Batista, A., and Kuehl, J., "On energy redistribution for the nonlinear parabolized stability equations method," *Fluids*, Vol. 7, No. 8, 2022, p. 264. https://doi.org/10.3390/fluids7080264.

[45] Liang, T., and Kuehl, J., "Validation of Porous Impedance Boundary Condition for a PSE code," AIAA Paper 2023-3290, 2023. https://doi.org/10.2514/6.2023-3290.

[46] Liang, T., Kafle, S., Khan, A. A., Paredes, P., and Kuehl, J., "On the inviscid energetics of Mack's first mode instability," *Theoretical and Computational Fluid Dynamics*, Vol. 37, No. 1, 2023, pp. 1–15. https://doi.org/10.1007/s00162-022-00636-9.

[47] Mittal, A., and Girimaji, S. S., "Mathematical framework for analysis of internal energy dynamics and spectral distribution in compressible turbulent flows." *Physical Review*, Vol. 4, No. 4, 2019, p. 042601. https://doi.org/10.1103/PhysRevFluids.4.042601.

[48] Chu, B., "On the Energy Tranfer to Small Disturbances in Fluid Flow (Part 1),," *Acta Mechanica*, Vol. 1, No. 3, 1965, p. 215.

[49] Vogel, E. A., and Coder, J. G., "A novel entropy normalization scheme for characterization of highly compressible flows," *Theoretical and Computational Fluid Dynamics*, Vol. 36, 2022, pp. 641–670. https://doi.org/10.1007/s00162-022-00617-y.

[50] Kuehl, J., "Thermoacoustic Interpretation of Second-Mode Instability," *AIAA Journal*, Vol. 56, No. 9, 2018, pp. 3585–3592. https://doi.org/10.2514/1.J057015.

[51] Beneddine, S., Sipp, D., Arnault, A., Dandois, J., and Lesshafft, L., "Conditions for Validity of Mean Flow Stability Analysis," *Journal of Fluid Mechanics*, Vol. 798, 2016, pp. 485–504. https://doi.org/10.1017/jfm.2016.331.